Energy & Environmental Science

Engineering metal-metal oxide surfaces for high-performance oxygen reduction on Ag-Mn electrocatalysts

Journal:	*Energy & Environmental Science*
Manuscript ID	EE-ART-01-2022-000047
Article Type:	Paper
Date Submitted by the Author:	06-Jan-2022
Complete List of Authors:	Zamora Zeledón, José; Stanford University, Chemical Engineering Kasun Kalhara Gunasooriya, G.; Technical University of Denmark, Physics Kamat, Gaurav; Stanford University, Chemical Engineering Kreider, Melissa; Stanford University, Chemical Engineering Ben-Naim, Micha; Lawrence Livermore National Laboratory Hubert, McKenzie; National Renewable Energy Laboratory Avilés Acosta, Jaime; Stanford University, Materials Science and Engineering Norskov, Jens; Technical University of Denmark, Physics Stevens, Michaela; Stanford University, Chemical Engineering Jaramillo, Thomas; Stanford University, Assistant Professor of Chemical Engineering

Engineering metal-metal oxide surfaces for high-performance oxygen reduction on Ag-Mn electrocatalysts

José A. Zamora Zeledón[a,b], G. T. Kasun Kalhara Gunasooriya[c], Gaurav A. Kamat[a,b], Melissa E. Kreider[a,b], Micha Ben-Naim[a,b,†], McKenzie A. Hubert[a,b], Jaime E. Avilés Acosta[b,d], Jens K. Nørskov[c], Michaela Burke Stevens[a,b,], and Thomas F. Jaramillo[a,b,*].*

a. Department of Chemical Engineering, Stanford University, 443 Via Ortega, Stanford, California 94305, United States

b. SUNCAT Center for Interface Science and Catalysis, SLAC National Accelerator Laboratory, 2575 Sand Hill Road, Menlo Park, California 94025, United States

c. Catalysis Theory Center, Department of Physics, Technical University of Denmark, 2800 Kongens Lyngby, Denmark

d. Department of Materials Science and Engineering, Stanford University, 496 Lomita Mall, Stanford, California 94305, United States

† Present Address: Materials Science Division, Lawrence Livermore National Laboratory, Livermore, California 94551, United States

KEYWORDS: alkaline electrochemistry, oxygen reduction, electrocatalysis, metal-metal oxide, silver-manganese.

ABSTRACT

Understanding fundamental material-property relationships in mixed-element catalyst systems is crucial to advancing the viability of renewable electrochemical energy technologies, an important part of creating a more sustainable future. Herein, we report our insight on the nature and dynamics of highly active silver-manganese oxide (Ag-MnO_x) catalyst surfaces for the oxygen reduction reaction (ORR) via a combined experimental-theoretical approach. Experimentally, we synthesize well-mixed Ag-Mn co-deposited thin films that are measurably flat and smooth, despite Mn surface migration and oxidation upon air exposure and electrochemical measurements. Cyclic voltammetry in 0.1 M KOH demonstrates up to 10-fold specific activity enhancements over pure Ag at 0.8 V vs. RHE for Ag-rich films (70 – 95 at% Ag in bulk). To further understand the Ag-Mn system, separate samples were synthesized with small amounts of Mn sequentially deposited onto the surface of a pure Ag thin film (Mn@Ag), ranging from partial to full surface coverage (down to 0.3 nm_{Mn} cm_{geo}^{-2} ~ 0.2 μg_{Mn} cm_{geo}^{-2}). These sequentially deposited Mn@Ag films show analogous performance to their co-deposited counterparts indicating similar enhanced active sites. With density functional theory (DFT), we calculate that this enhancement arises from the tuned *d*-band of these material surfaces owing to the optimal hybridization of the electronic structures in specific Ag and MnO_x geometries. Together, electrochemical measurements, DFT calculations, x-ray absorption spectroscopy, and valence-band x-ray photoelectron spectroscopy suggest synergistic electronic interactions between Ag and MnO_x yields enhanced oxygen adsorption, and thus ORR activity, with DFT highlighting the Ag–MnO_x interface sites as the most enhanced. This work demonstrates how combined experimental-theoretical methods can help design electrocatalysts with enhanced electrocatalytic properties and understand the nature of complex mixed metal-metal oxide surfaces.

BROADER CONTEXT

Electrochemical energy conversion technologies are key to ensuring a renewable and sustainable future. Technologies such as fuel cells, metal-air batteries, and electrolyzers help decarbonize and

diversify the energy landscape. These technologies rely on electrocatalyst materials to covert between electrical and chemical energy. Understanding surface phenomena leading to enhanced electrocatalytic properties is necessary to advance the rational design of optimal catalyst interfaces and improve the efficiency of electrochemical energy conversion technologies. In this work, via physical vapor deposition, we engineer silver-manganese electrocatalysts which develop electrolytically enhanced Ag-MnO_x surfaces that afford up to 10-fold alkaline oxygen reduction activity improvements over pure Ag. Density function theory modeling of several possible active sites suggests that Ag-MnO_x interface sites are likely the most enhanced in the system. In addition to demonstrating that metal-metal oxide surfaces can yield promising electrocatalyst active site motifs, we show Ag-MnO_x can provide robust $4e^-$ selective ORR that may be suitable for adoption, i.e., in metal-air batteries and anion exchange membrane fuel cells. Central to this study is a combined experiment-theory approach, widely translatable to other electrocatalytic systems, to uncover fundamental insight about the possible physical phenomena, i.e. active site geometry, leading to synergistic catalysis at complex metal-metal oxide surfaces.

1. INTRODUCTION

The electrochemical reduction of oxygen, or, the oxygen reduction reaction (ORR), is key in emerging renewable energy conversion and storage technologies such as fuel cells and metal-air batteries. These and many other sustainable energy technologies have great promise to significantly decrease greenhouse gas emissions from the transportation and energy sectors, thus mitigating the detrimental impact of climate change on humanity and the environment.[1, 2] Owing to the large overpotential needed to drive the ORR, the development of durable, cheaper, and more active catalysts is needed to promote the growth and diversification of fuel cell technology.[3, 4] Alkaline environments enable the use of many materials that would be electrochemically unstable at relatively low overpotentials in acidic media and enable the use and study of non-Pt materials,[5, 6] thus helping to diversify the range of viable electrocatalyst materials. Ag-based catalysts, specifically bimetallics, have gained interest over the last decade and have shown promising enhanced performance when mixed, for instance, with Pd[7-11], Mo[12], Cu[13, 14], Sn[15], Co[16], and Mn[17-25] for the ORR in alkaline conditions. Moreover, Ag alone has suitable intrinsic activity and nearly complete $4e^-$ selectivity,[3, 26, 27] in addition to being about two orders of magnitude cheaper than Pt

or Pd (the most active single metals for ORR),[8, 28, 29] thus making Ag-based materials highly promising to diversify electrocatalysts for renewable electrochemical energy conversion and storage technologies such as fuel cells and metal-air batteries.[8]

Ag-Mn-based electrocatalysts are of particular interest because they have shown promising performance for the ORR[17-25] and Mn is cheap, abundant, and can be a good ORR catalyst on its own[30-35]. Notably, for these systems, surface Mn, whether synthesized as Mn oxide or pure Mn metal/metallic Ag-Mn (i.e. in vacuum), is reported to be Mn oxide (MnO_x) after contact with air owing to the strong oxophilicity of Mn.[17-25, 30-33, 36-38] However, while there is substantial evidence of overall ORR performance enhancements in Ag-Mn systems, several different phenomena have been hypothesized to explain the improved performance. For instance, it has been proposed that Ag nanoparticles supported on Mn_3O_4/C show enhanced performance owing to the electronic interactions between the catalyst and its support, as well as support-induced strain.[18] Highly dispersed Ag and Mn_3O_4/C nanoparticles have been suggested to yield enhanced ORR activity due to ligand and ensemble effects when the components are in close proximity.[17, 24] Others have proposed that Ag can form Ag–Mn–O bonds in silver-manganese oxide composites (i.e. silver-manganese oxide nanofibers and Ag-MnO_x/graphene) resulting in induced defects that promote the adsorption of oxygen.[22, 25] The differences in enhancement mechanism for these Ag-Mn systems highlight the difficulty in comparing intrinsic electrocatalytic activity among catalysts with different morphologies and emphasize the need to continue probing the origin and intrinsic nature of these enhancements. Furthermore, while precious group metals (PGMs) mixed with Ag, such as Pd[7-11], have reasonable material stability under electrochemical conditioning, Ag-mixtures with more abundant cheaper first-row transition metals, such as Cu[13, 14], can undergo substantial surface composition and/or oxidation state changes concurrent with increased activity. Deconvoluting the individual roles of ligand, strain, and ensemble effects, in such complex materials is therefore complicated, but vital for understanding the nature of the active site(s) and rationally advancing surface-centric catalyst design. To this end, surface-specific studies with well-characterized and controlled materials and electrochemical environments would not only improve our fundamental understanding of Ag-based active sites for the ORR, but also broaden our abilities to engineer metal-metal oxide surfaces with tuned electrocatalytic properties.

Herein, we investigate how the nature of the chemical interactions between Ag, MnO_x, and O-based adsorbates can yield highly active ORR active sites for certain combinations of Ag and Mn. By employing co- and sequential- physical vapor deposition synthesis approaches and utilizing thorough physical and electrochemical characterization, we report Ag-MnO_x surfaces on Ag-Mn catalysts with enhanced ORR specific activity and identify important redox behaviors/dynamics. All films are smooth with homogeneous surface compositions. Upon contact with air after synthesis, we observe Mn oxidize in all films and enrich the near-surface region of the co-deposited films. For comparison, in the Mn@Ag configuration, we deposit films ranging from full (e.g. Mn_{10nm}@Ag) to partial (e.g. $Mn_{0.3nm}$@Ag) Mn surface coverage. We see that various as-deposited Ag-rich thin film compositions (co- and sequential- deposition) can yield similar enhanced ORR activities possibly due to the presence or formation of comparable active sites on the Ag-MnO_x surface. Specifically, co-evaporated mixed Ag-Mn and sequentially evaporated Mn@Ag thin films with partial Ag surface coverage yield nearly identical performance down to ~ 1 at% Mn near-surface content. Using experimental data and density functional theory (DFT), we propose that the enhancement comes from an optimized electronic structure and O adsorption strength from cooperative interactions between Ag and MnO_x, with DFT indicating Ag–MnO_x interface sites are the most enhanced. Altogether, we demonstrate how theory and experiment can complement each other to gain fundamental insight about material-property relationships that are needed to engineer optimal active sites.

2. MATERIALS AND METHODS

2.1. Experimental Methods

Synthesis. The electron beam (*e*-beam) physical vapor deposition (PVD) synthesis techniques (co- or sequential- deposition) and material characterization techniques employed here are similar to those in our previous work.[8] Ag (99.99% purity in vitreous carbon crucible, Kurt J. Lesker), Mn (pieces, 99.95% purity in W crucible, Kurt J. Lesker), Ag-Mn thin films (Ag_xMn_{1-x} where x (%) = 0, 30, 70, 90, 95, and 100 and Mn_y@Ag_{70-y} (Mn onto Ag) where y = 0.3, 1, 5, and 10 nm) were synthesized via *e*-beam PVD (at < 3.0 x10^{-6} torr) using a custom made PVD system (Technical Engineering Services) equipped with a center thermal source, two side electron beam *e*-beam sources, and a rotating stage. For each source, independently calibrated quartz crystal

microbalances (QCMs) precisely and accurately measure the deposition rate, allowing for careful and reproducible control of film composition and thickness. Before deposition, pre-polished 5 mm diameter glassy carbon disks (HTW Hochtemperatur-Werkstoffe GmbH) were cleaned by sequential sonication for 30 min in soapy water, acetone, ethanol, and isopropanol and subsequently rinsed with pure Millipore water (R = 18 MΩ cm). Next, they were loaded with double sided Kapton tape to a 10 cm diameter dummy Si wafer and mounted to the rotating stage. We synthesized 70 nm thick Ag-Mn thin films with individual deposition rates (≤0.12 nm s^{-1} individually) set to achieve the desired bulk Ag_xMn_{1-x} composition. For the Ag_xMn_{1-x} thin films, we initially chose evaluated x (%) = 0, 30, 70 and 100 to screen the performance of the pure materials and representative high and low Ag-Mn compositions, followed by x (%) = 90, 95 to try to further optimize performance based on the results in this work. For $Mn_y@Ag_{70-y}$ Ag was evaporated at a 0.12 nm s^{-1} rate, and Mn was evaporated at 0.01 nm s^{-1} for y = 0.3 and 1 nm and 0.05 nm s^{-1} for y = 5 and 10 nm. The electron beam(s) sweep pattern was hour-glass shaped. All the samples were stored and transported in air. In addition to the standard pre-evaporation during power ramp up and soak during the deposition recipe, the Mn target was pre-evaporated, in manual mode, with the target shutter closed to evaporate/eliminate the Mn-oxide capping layer that forms on the target upon venting of the deposition high vacuum chamber, and therefore be able to evaporate Mn metal.

Physical Characterization. X-ray photoelectron spectroscopy (XPS) was performed using a PHI III Versaprobe equipped with Al Kα radiation (1486 eV). Pass energies of 224 eV (0.8 eV step, 20 ms dwell time) and 55 eV (0.1 eV step, 20 ms dwell time) were used to collect survey (Su) and high resolution (HR) spectra, respectively, on the films deposited on glassy carbon disks. The instrument's neutralizer and Ar^+ gun in neutralizing mode were used for all measurements. The sample-to-detector angle was 45° (default), and the x-ray beam was perpendicular to the sample. A 100 μm × 100 μm high power spot (100 W, 20 KV) was used, and the spot location was set to approximately the center of the samples. Depth profiling XPS (224 eV pass energy, 200 μm × 200 μm Ar^+ sputtering, power varied to control sputtering rate) was performed on the thin films before and after ORR testing to investigate composition as a function of depth. The stage height was aligned for each sample to maximize signal intensity. Compositional quantification and fitting of XPS spectra was done using CasaXPS[39] software. Tougaard background corrections were used to

calculate the area under the Mn 2*p* (or Mn $2p_{3/2}$), Ag 3*d*, and O 1*s* peaks (manually selected energy range) to subsequently calculate their near-surface atomic composition (with sensitivity factors: $S_{Ag,3d} = 18.04$ and $S_{Mn,2p} = 13.91$, $S_{Mn,2p3/2} = 9.17$, $S_{O,1s} = 2.93$). The Mn $2p_{3/2}$ peaks, with a Shirley background correction, were fitted according to guidelines and initial peak separation ranges, full width half maxima (FWHM), and peak area ratios constraints reported before;[40] the FWHM was allowed to relax to achieve a good fit. Mn oxidation state was further probed via Mn 3*s* HR XPS.[40] XPS spectra were aligned by setting the C 1*s* peak to 284.8 eV. Valence band (VB) XPS (20 eV pass energy, 0.05 eV step, 50 ms dwell time), and complementary Su (200 eV pass energy, 1 eV step, 20 ms dwell time) and HR Mn 2*p*/Ag 3*d*/C 1*s*/O 1*s* (20 eV pass energy, 0.1 eV step, 50 ms dwell time) XPS of the as-deposited thin films grown on a Si(111) wafer and employing a 400 μm × 400 μm x-ray spot (neutralizer off) were performed on a Thermo Fisher K-Alpha Plus XPS at the Molecular Foundry, Lawrence Berkeley National Laboratory. VB XPS measurements (25 cycles) were collected before and after Ar^+ sputtering cleaning of the surface, which was required to remove the VB contributions of adventitious carbon. The monatomic Ar^+ sputtering energy and time were calibrated on a separate sample spot to determine the minimum power and time needed to remove the C 1*s* from the Su and HR spectra without significantly changing sample (XPS) composition and oxidation state; broadly, we cleaned the surface with an Ar^+ sputtering energy 2000 eV for no more than 45 seconds and generally noticed the more Ag-rich samples were more easily sputtered. Using Thermo Fisher's Avantage software, the VB XPS data files were exported and processed in CasaXPS[39]. The BE for both the spectra before and after surface cleaning was aligned by setting the before-cleaning C 1*s* peak to 284.8 eV. A Shirley background subtraction was applied as done previously for samples involving metal oxides.[41-43] We use Matlab trapezoidal integration to calculate the VB-area and define the VB-center as the as a weighted mean energy of the spectrum[44] in the BE range of interest (see more details in **Supplementary Table S5**). VB spectra were normalized by setting the maximum peak intensity equal to 1 arb. unit. *Ex situ* x-ray absorption spectroscopy (XAS) was performed, in vacuum, at beamline 8-2 at the Stanford Synchrotron Radiation Light Source at SLAC National Accelerator Laboratory. The total electron yield (TEY) was averaged from 5 to 10 scans. All XAS data was processed and edge-jump normalized using Larch[45] software. Elemental mapping of Ag and Mn was performed by scanning Auger electron spectroscopy (AES) and SEM-energy dispersive spectroscopy (SEM-EDS). AES measurements were conducted on a PHI 700 Scanning Auger Nanoprobe with a 10 kV, 10 nA

electron beam. SEM-EDS characterization utilized a Thermo Fisher Scientific Apreo S LoVac with a Bruker Quantax EBSD 400i integrated system containing an XFlash 6 | 60 SDD EDS detector, using beam parameters of 20 kV, 1.6 pA (unless otherwise noted). Using a Park Systems XE-70 instrument equipped with a premounted MikroMasch HI'RES-C14/Cr-Au probe ($\leq$ 2 nm tip radius), we obtained 5 μm × 5 μm (or larger) size non-contact atomic force microscopy (AFM) images in at least triplicate at random places on the sample and calculated topographical information using Gwyddion[46] software. Cu Kα (λ = 0.154 nm) grazing incidence x-ray diffraction (GI-XRD) measurements were collected with an X'Pert Pro PANalytical Materials Research diffractometer. We collected grazing incidence (ω = 1°) measurements using a 20 mm beam mask and a 1/2 mm divergence slit. All diffractograms of as-deposited films were collected on Ag-Mn thin films grown on standard glass slides to increase the area of material under illumination and eliminate background interferences from glassy carbon substrates. Diffractograms were normalized by the maximum peak intensity and corrected by a multi-point linear background subtraction. Post-electrochemical (removed from electrolyte at the open circuit potential and rinsed with Millipore water (R = 18 MΩ cm)) physical characterization (AES, SEM-EDS, XPS, AFM) was performed on thin films within 2 weeks of activity testing (stored in air).

Electrochemical Evaluation. Cyclic voltammetry (CV) electrochemical characterization was performed by rotating disk electrode (RDE, 1600 rpm, 20 mV s^{-1}) testing using a Pine Research Instruments rotator setup and a Biologic VMP-300 potentiostat. We used 0.1 M KOH as the electrolyte, made from semiconductor grade pellets (Sigma Aldrich, 99.99% trace metals basis) and Millipore water (R = 18 MΩ cm). We used a three-electrode cell with a graphite rod (placed into a jacket with a porous frit to mitigate carbon contamination of the working electrolyte) counter electrode and either an RHE (reversible hydrogen electrode; flame annealed, clean, coiled Pt wire jacketed in a porous tube with H_2-saturated electrolyte and active H_2 sparging) or a Ag/AgCl (accumet, epoxy body; calibrated to an RHE before and after electrochemical measurements) reference electrode. The Ag-Mn thin films deposited on glassy carbon disks were mounted in a Teflon RDE tip (Pine Research Instruments) and used as working electrodes. All polarization measurements in O_2-saturated electrolyte were manually corrected for the uncompensated electrolyte resistance (R_u, measured by potential electrochemical impedance spectroscopy (PEIS)) and background non-ORR contributions measured by CV in N_2-saturated electrolyte (after

sparging N_2 for 5 min) immediately after the last CV cycle in O_2-saturated electrolyte (unless otherwise noted). The activity for the ORR was evaluated by cyclic voltammetry at 20 mV s^{-1} from ~ 1 to 0 V vs. RHE. Using thin films, no more than 2 weeks old, we performed 20 CV cycles in O_2-saturated electrolyte (O_2 CVs), followed by 2 CVs in N_2-saturated electrolyte (N_2 CVs) to correct for non-ORR currents and to evaluate the electrochemical/redox characteristics of the Ag-Mn films in the absence of O_2 in the potential range of interest. Rotating ring disk electrode (1600 rpm, 20 mV s^{-1}) measurements were collected on select samples to quantitatively investigate the selectivity of Ag-Mn thin films (Pt ring held at 1.2 V vs. RHE, $N_c = 0.22$ as calibrated in house via the ferricyanide/ferrocyanide redox couple).[47] The R_u was measured before and after electrochemical cycling and generally ranged between 30 – 40 Ω for all samples. For each experiment, the R_u value remained consistent before and after ORR (to within approximately 5 Ω).

2.2 Theory & Computational Methods

Periodic spin-polarized density functional theory (DFT) calculations were performed using the RPBE functional,[48] a plane-wave basis set with a cutoff kinetic energy of 500 eV, and the projector-augmented wave method,[49] as implemented in the Vienna Ab-initio Simulation Package (VASP version 5.4.4).[50] The pure Ag surface was modeled as a five-layer p(3 × 3) Ag(111) fcc slab with RPBE optimized lattice constant of 4.219 Å and the Brillouin zone was sampled with a Γ-centered (3 × 3 × 1) Monkhorst−Pack grid.[51] Metallic Ag_xMn_{1-x} thin films were modeled as five−layer p(2 × 2) (111) fcc slabs with optimized lattice constants of $Ag_{75}Mn_{25}$ (4.171 Å), $Ag_{50}Mn_{50}$ (4.111 Å), and $Ag_{25}Mn_{75}$ (4.032 Å) and the Brillouin zone was sampled with a Γ-centered (5 × 5 × 1) Monkhorst−Pack grid. To model MnO_x stripes and nano-islands, a three-layer *p*(6 × 6) Ag surface model and a (1 × 1 × 1) Monkhorst−Pack grid was used. The top three layers for the five-layer slabs and top two layers for the three-layer slabs, MnO_x stripes and nano-islands, and adsorbed species were fully relaxed, whereas the bottom layers were constrained at their corresponding bulk positions. The slabs were separated in the perpendicular *z* direction by 15 Å of vacuum, and a dipole correction was applied. A Hubbard U correction of 3.9 eV was applied for all Mn atoms in the MnO_x stripes and nano-islands.[52] The electronic and force convergence criterion were 10^{-5} eV was 0.05 eV $Å^{-1}$, respectively.

Catalytic activities of the different surface structures were evaluated based on the theoretical limiting potential for ORR (U_L), defined as the highest potential at which all the reaction steps become exergonic by assuming an association reaction mechanism with *OOH, *O, and *OH (where the asterisk indicates surface adsorbed species) as reaction intermediates.[53] The adsorption free energies, ΔG_x (for x=*OOH, *O, and *OH), of the adsorbates are calculated as $\Delta G_x = \Delta E_{DFT} + \Delta E_{ZPE} + \int_0^{298.15} C_p dT - T\Delta S$, where ΔE_{DFT} is the difference in DFT calculated electronic energy, ΔE_{ZPE} is the difference in zero-point energies, $\int_0^{298.15} C_p dT$ is the difference in integrated heat capacity from 0 to 298.15 K, ΔS is the change in entropy of the adsorbed species, and calculated with respect to the catalyst surface, relative to H_2O(g) and H_2(g) at $U = 0$ V vs. the computational hydrogen electrode (CHE) and standard conditions (T = 298.15 K and P = 1 bar). The ($\Delta E_{ZPE} + \int_0^{298.15} C_p dT - T\Delta S$) values[54] and solvation corrections[55] were taken from our previous work and subsequently added to all the adsorption calculations. The difference between the equilibrium potential of U = 1.23 V vs. CHE and the limiting potential is referred as the theoretical overpotential (η), i.e. $\eta = 1.23\ V - U_L$. Lower η or higher U_L indicate improved theoretical ORR activity. It is important to note that η should not be compared directly with a measured overpotential, since the measured overpotentials depend on the current density.[55]

3. RESULTS & DISCUSSION

3.1 Physical Characterization and Electrochemical Evaluation of Enhanced ORR on Co-deposited Bimetallic Ag-Mn Thin Films

Studying fundamental material property-activity relationships requires the synthesis of well-controlled catalyst systems. While Ag and Mn are not thermodynamically miscible,[56] mixed Ag-Mn materials have been synthesized previously as nano-particulates[17-25, 38]. We employed *e*-beam PVD to co-deposit 70 nm Ag-Mn thin films of various compositions as this technique produces well-mixed bimetallics and has the potential to yield meta-stable alloyed phases of

thermodynamically immiscible materials such as Ag-Cu[14] and Ag-Ni[57].[8] These Ag_xMn_{1-x} thin films, where x (%) = 0, 30, 70, 90, 95, and 100, were characterized using x-ray diffraction, x-ray spectroscopies, and microscopies to investigate crystal structure, composition, electronic structure, and morphology/topography. Subsequently, to investigate the ORR behavior and final state of the Ag_xMn_{1-x} thin films, cyclic voltammetry (CV) under O_2-staturation (O_2 CVs, 20 cycles unless otherwise noted, 1600 rpm, 1 – 0 V vs. RHE, 20 mV s^{-1}) and CV under N_2-saturation (N_2 CVs, 2 cycles, 1600 rpm, 1 – 0 V vs. RHE, 20 mV s^{-1}), followed by post-ORR testing physical characterization, was performed.

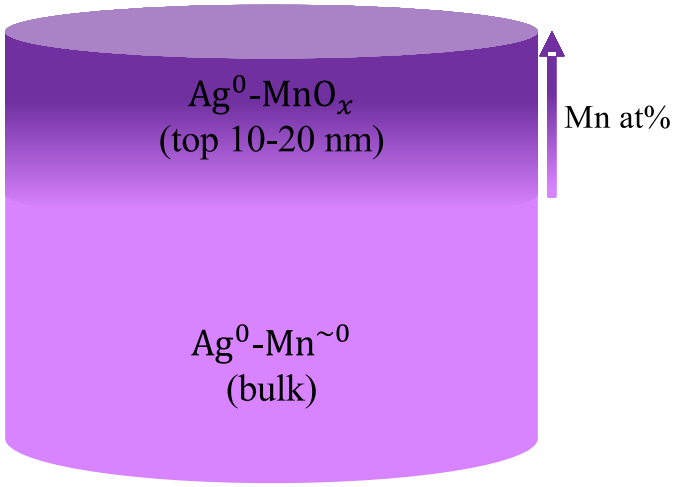

Figure 1. Sketch illustrating the physical characteristics of the co-deposited Ag-Mn thin films both before and after electrochemical experiments based on extensive physical characterization measurements of topography, structure, composition, and oxidation state. The main differences of the films post-ORR are that Mn is in a more oxidized state and has partially leached. Post-ORR, owing to the partial Mn-leaching, the near-surface for $Ag_{70}Mn_{30}$, $Ag_{90}Mn_{10}$, and $Ag_{95}Mn_5$ is enriched with Ag, relative to the initial pre-ORR composition, however the surface is still Mn-enriched relative to the bulk. See the XPS near-surface composition of the thin films before and after ORR in **Table 1**.

Table 1. Elemental Ag/Mn quantification (from XPS, see details in **Supplementary Figure S1-S4** and **Table S1**) of representative Ag_xMn_{1-x} thin films before and after ORR testing. We define near-surface as the operating XPS probe depth, which is on the order of a few nanometers, and can vary slightly as a function of the composition of the volume being probed.

As-evaporated	Air-exposed		Post-ORR	
Nominal Bulk Sample Composition	Near-Surf.	Near-Surf.	Near-Surf.	Near-Surf.

	$\frac{Ag}{Ag+Mn}$ (at%)	$\frac{Mn}{Ag+Mn}$ (at%)	$\frac{Ag}{Ag+Mn}$ (at%)	$\frac{Mn}{Ag+Mn}$ (at%)
Mn	0	100	0	100
$Ag_{30}Mn_{70}$	5	95	2	98
$Ag_{70}Mn_{30}$	36	64	59	41
$Ag_{90}Mn_{10}$	60	40	88	12
$Ag_{95}Mn_{5}$	84	16	97	3
Ag	100	0	100	0

It is essential to first physically understand the catalyst material itself to understand trends in electrocatalytic performance. Owing to the complex nature of our Ag_xMn_{1-x} thin films, we briefly summarize the key results from extensive physical characterization, which affirm that the samples consist of a smooth, well-mixed Mn-oxide rich surface as measured immediately after synthesis and air exposure (**Figure 2a-h**). Further on, we discuss the surfaces after ORR electrocatalysis. A comprehensive discussion of all results is available in **Supplementary Note S1**.

Compositionally, together with XAS (**Figure 2b**) and XPS (**Figure 2c-e**, **Supplementary Figure S1-S4** and **Table S1**), we observe that after air exposure, Mn is in an oxidized state (therefore referred to as MnO_x) in the near-surface region, while in the bulk Mn remains largely metallic for the pure Mn sample and all of the mixed Ag_xMn_{1-x} thin films. In agreement with calculated DFT segregation thermodynamics (**Supplementary Tables S2**,**S3**), XPS indicates that concomitant with Mn surface oxidation upon air exposure (Mn $2p_{3/2}$ fit to mostly (> 50 %) Mn^{2+} shown in **Figure 2c**, **Supplementary Figure S4** and **Table S1**), the near-surface region is also enriched with Mn (~10 – 40 % enrichment) relative to the bulk content owing to Mn migration towards the surface within the top ~10-20 nm (**Figure 2d**,**e**). Mn $2p_{3/2}$ peak fitting (**Supplementary Figure S4** and **Table S1**) suggests that, on average, the valency of near-surface Mn slightly increases with increased Ag content, going from ~+2.2 for the pure Mn film to ~+2.6 for $Ag_{90}Mn_{10}$ and $Ag_{95}Mn_5$ (**Figure 2c**). GI-XRD (**Figure 2a**) reveals that the presence of Mn has a negligible effect on the bulk face centered cubic (fcc) crystal structure of Ag, as all Ag_xMn_{1-x} films have a strong peak at 38.2° corresponding to the (111) peak of Ag.[8] Only the lower-Ag-content $Ag_{30}Mn_{70}$ film has an additional small shoulder peak corresponding to the (411) α-Mn metal body-centered cubic (bcc) phase as seen at 43.0° for the pure Mn film (see reference pattern in **Supplementary Figure S5**).

With AES (**Figure 2f** and **Supplementary Figure S6**), we see well-mixed (within tens of nanometers resolution) Ag and MnO_x in the near-surface of the Ag_xMn_{1-x} thin films, and with SEM-EDS (**Supplementary Figure S7**) we observe well-mixed (within microns resolution) Ag and Mn in the bulk. AFM (**Figure 2g**, **Supplementary Figure S8** and **Table S4**) indicates the films are flat and smooth (roughness factors (RFs) $\leq$ 1.01 and root mean square roughnesses (RMSRs) ~2–5 nm), with exposed surface areas approximately equal to the geometric electrode area. The shape of the total electron yield (TEY) Mn $L_{3,2}$ XANES ($2p \rightarrow 3d$ transition, probing the top ~10 nm) is indicative of an Mn^{2+} (MnO) dominant valency.[37] Moreover, the $L_{3,2}$ area decreases with Ag content suggesting that the Mn *d*-holes of the Ag_xMn_{1-x} thin films decrease with increased Ag content (**Figure 2b** and **Supplementary Figure S9**). XPS supports this electronic hybridization as seen by the negative (up to ~ 0.5 eV) shift of the Ag 3*d* peaks in **Figure 2h** when Ag is mixed with Mn and further suggests that the near-surface mixed Ag-MnO_x can result in upshifted *d*-bands relative to Ag, in agreement with valence band (VB) XPS (**Supplementary Figure S10** and **Table S5**) results that are discussed further below together with theoretical modeling efforts. **Figure 1** illustrates the material state of our Ag_xMn_{1-x} thin films after synthesis and air-exposure, both prior to and after electrochemical evaluation. **Table 1** summarizes the representative as-deposited (air-exposed) and post-ORR Ag_xMn_{1-x} thin film trends in XPS near-surface Ag-Mn composition.

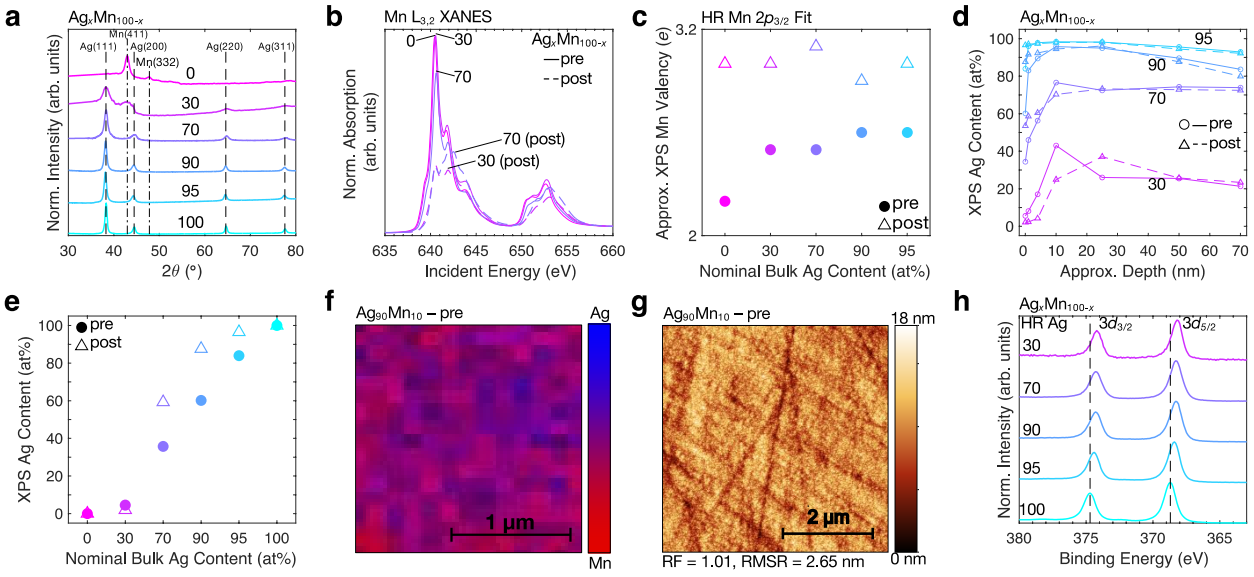

Figure 2. (**a**) Representative GI-XRD of the as-deposited Ag_xMn_{1-x} thin films (grown on standard glass slides to increase area of x-ray illumination and avoid background interferences from glassy carbon); measured Ag fcc peak positions are shown by dashed (--) lines and the α-Mn bcc peak positions are shown by dash-dot (-.) lines. (**b**) Representative Mn $L_{3,2}$ XANES of as-deposited (–) and post-ORR testing (--) $Ag_{70}Mn_{30}$ and $Ag_{30}Mn_{70}$ thin films, along with a control as-deposited Mn thin film (for XAS specifically, the post-ORR samples underwent 7 O_2 and 2 N_2 CV cycles from 1 – 0 V vs. RHE at 20 mV s^{-1}). (**c**) Average Mn oxidation state (valency) of Ag_xMn_{1-x} thin films before (circles) and after (triangles) ORR testing according to the Mn $2p_{3/2}$ XPS fit (see more valency details Supplementary **Figures S1,S3,S4**, **Tables S1, S5** and **Note S1**). (**d**) Depth profile XPS elemental compositional analysis before (circles,-) and after (triangles,--) ORR testing of Ag_xMn_{1-x} thin films (lines for visual guidance only). (**e**) Near-surface XPS elemental compositional analysis before (circles) and after (triangles) ORR testing of Ag_xMn_{1-x} thin films. (**f**) Representative AES mapping of as-deposited $Ag_{90}Mn_{10}$ showing the overlayed signal (intensity) of Ag (blue) and Mn (red). (**g**) Representative AFM topography images of as-deposited $Ag_{90}Mn_{10}$. (**h**) HR Ag 3*d* XPS of the as-deposited Ag_xMn_{1-x} thin films; dashed lines at the pure Ag $3d_{3/2}$ (374.7 eV) and $3d_{3/2}$ (368.7 eV) peak positions. Samples/nominal compositions (*x*) are color coded in (**a**–**e**,**h**) consistent with the explicit in-figure text labels.

Taken together, the *ex situ* physical characterization of the as-deposited (air-exposed) Ag_xMn_{1-x} thin films supports a model where the near-surface is flat/smooth, well-mixed, and Mn-oxide-rich, while the bulk is well-mixed, metallic, and of the intended as-evaporated nominal composition with mostly fcc crystallinity most similar to that of pure Ag. For simplicity, we will refer to the Mn at or near the surface as MnO_x, referring broadly to a variety of Mn-oxides, as opposed to the metallic Mn in the bulk. In addition, the thin films could be described in terms of both their approximate near-surface (in air as measured by *ex situ* XPS on representative samples, **Figure 2e**) and nominal bulk (as-evaporated in vacuum, as measured *in situ* with quartz crystal microbalances) compositions as shown in **Table 1**; for simplicity we will refer to the catalysts based on their nominal as-evaporated in vacuum bulk composition. This complicated near-surface highlights that, in the context of catalysis, such materials could exhibit a variety of possible active sites, namely Ag, MnO_x, and/or Ag–MnO_x interfacial sites, which will be discussed in the next sections.

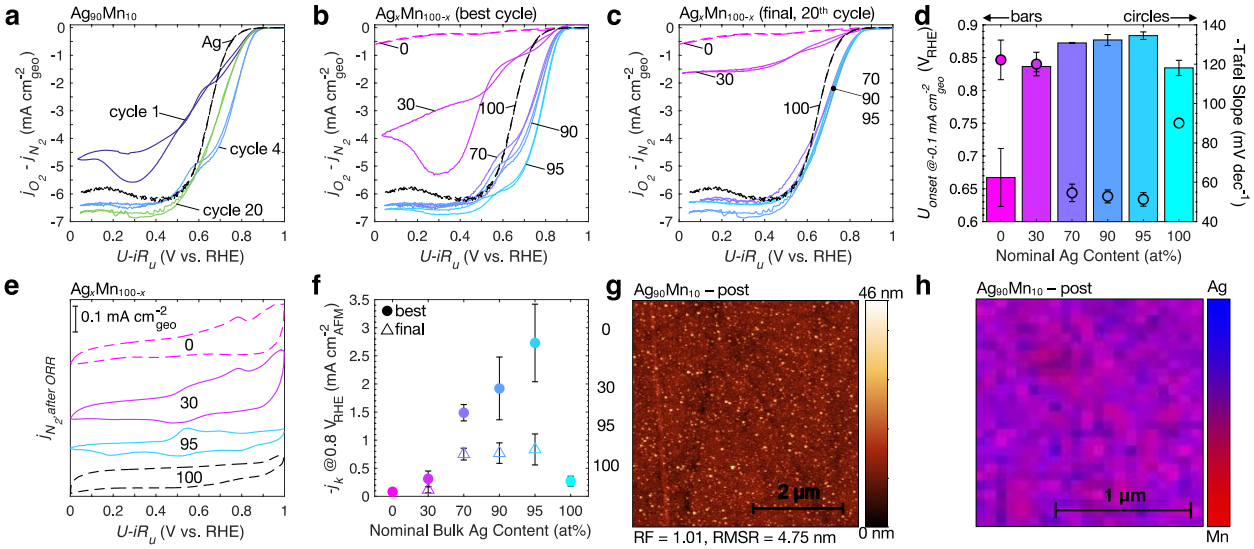

Figure 3. (**a**) Representative ORR CV cycling showing of $Ag_{90}Mn_{10}$ showing cycle 1 (green), cycle 4 (blue), and cycle 20 (purple) (see all cycles in **Supplementary Figure S11**). Representative (**b**) best and (**c**) final (20th) cycle ORR CV for Ag_xMn_{1-x} thin films (see detailed cycling in **Supplementary Figure S11**). (**d**) Best cycle average onset potential (bars, left y-axis) and Tafel slope (circles, right, y-axis) of the Ag_xMn_{1-x} thin films. (**e**) Representative characteristic (in N_2-saturation) CV for select Ag_xMn_{1-x} thin films after 20 ORR cycles. CV in **a**–**c**,**e** at 20 mV s^{-1} and 1600 rpm (see more details in **Supplementary Figure S14**). (**f**) Average kinetic current density (specific activity) for the best (triangles) and final (circles) CV cycles at 0.8 V vs. RHE of Ag_xMn_{1-x} thin films normalized by AFM roughness post-ORR evaluation. (**g**) Representative AFM topography images of $Ag_{90}Mn_{10}$ after ORR cycling. (**h**) Representative AES Ag/Mn mapping of $Ag_{90}Mn_{10}$ after ORR testing. Post-ORR is 20 O_2 and 2 N_2 CV cycles from 1 – 0 V vs. RHE at 20 mV s^{-1}). Samples/nominal compositions (x) are color coded in (**a**–**f**) consistent with the explicit in-figure text labels. Error bars correspond to the standard deviation of at least three separate measurements.

Understanding the nature of the ORR activity on materials with well-characterized structure and composition is important to aid in the design and development of catalysts with optimal ORR performance. As exemplified by **Figure 3a**, within the applied potential range utilized in this work, the ORR CV performance of the mixed Ag_xMn_{1-x} thin films varies upon cycling. Specifically, with cycling the average onset potential ($j_{O_2-N_2}$ = –0.1 mA cm_{geo}^{-2}, averaged in triplicate, average of anodic and cathodic sweeps) hits a maximum around cycle 3 to 5 and then slowly decreases until the cycles begin to converge by the final (20th) tested cycle (see also **Supplementary Figure S11**). The best (3rd – 5th) and the final (20th) ORR CVs for the mixed Ag_xMn_{1-x} films is shown in **Figure 3b** and **2c**, respectively. For consistency the converged Mn CV (20th cycle) and the 3rd Ag CV

cycle are used for comparison throughout this work (see all cycles for representative samples in **Supplementary Figure S11**).

The Ag ORR CV is reproducibly in agreement with our previous work,[8, 14] with an onset potential of ~ 0.83 V vs. RHE (**Figure 3b–d**). Moreover, while the ORR CVs for Ag show consistent performance over 20 cycles (**Supplementary Figure S11b**), the Mn thin film ORR CVs require ~8 cycles (**Supplementary Figure S11a**) to stabilize/converge and only reach low diffusion-limited current density magnitudes of about –1.3 and –0.6 mA cm_{geo}^{-2} on the 1st and 20th cycles, respectively, with an average onset potential ~0.67 V vs. RHE at the 20th cycle (**Figure 3b–d**), which are lower than those of most forms of Mn-oxide catalysts reported[17, 19-22, 30-33, 58] in the literature. While the ORR performance of this Mn thin film is poor compared to other forms of Mn-oxide catalysts reported[17, 19-22, 30-33, 58], the ORR CV profile of our Mn thin film resembles that of a similarly inactive MnO deposited by atomic layer deposition (ALD) onto a glassy carbon support.[30] Therefore, based on the *ex situ* XPS (**Figure 2c** and **Supplementary Figure S1-S4,S10** and **Table S1**,**S5**) and XAS (**Figure 2b**) characterization of the Mn film before electrochemical testing and the measured Mn ORR profile (**Figure 3b**,**c** and **Supplementary Figure S11a**), we hypothesize that the initially dominant surface Mn-oxide species during ORR testing of our Mn thin film might be MnO, which has been previously noted as the least ORR active Mn-oxide.[23] However, it is important to note that manganese oxides are known to be capable of transforming within the potential range investigated in this work (1–0 V_{RHE}) and that the starting material valency can have a big impact on the resulting surface during reaction.[30, 36, 59, 60]

Looking at the best ORR performance of the Ag_xMn_{1-x} thin films (**Figure 3b**,**d**), we find two main material-performance motifs, namely Mn-like overall performance for the Ag-poor (x = 30) thin film (onset potential ~0.84 V vs. RHE), and enhanced performance for the Ag-rich (x = 70, 90, 95) thin films, with onset potentials ~0.88 V vs. RHE (~40 mV higher than pure Ag). Tafel slope analysis (**Figure 3d**) further distinguishes the Ag-rich and Ag-poor performance motifs. Specifically, the $Ag_{30}Mn_{70}$ film has a Tafel slope of ~110 mV dec^{-1}, which is close to that observed for Mn (~125 mV dec^{-1}), suggesting similarities in mechanism, selectivity, and/or active site. In contrast, the Tafel slopes (**Figure 3d**) of the Ag-rich thin films are 50-60 mV dec^{-1}, similar to those seen on high performing Pt- or Pd-based materials,[8, 61-63] suggesting improved activity

compared to the 90 mV dec^{-1} Tafel slope seen on pure Ag, as well as differences in mechanism, active site, and/or adsorbates, among other potential factors.

Looking more closely at the compositional-activity motifs, while the Ag-poor thin film ($Ag_{30}Mn_{70}$) exhibits an improved onset potential (**Figure 3b**,**d**) and mass transport limited current density compared to the Mn film, the overall performance and profile does not resemble that of an active, $4e^-$ selective, ORR catalyst such as the Ag thin film. In fact, RRDE selectivity measurements of $Ag_{30}Mn_{70}$ show an average ~30% H_2O_2 selectivity at the average ORR onset potential of ~ 0.84 V vs. RHE, in contrast to the near 0% H_2O_2 selectivity of Ag and $Ag_{70}Mn_{30}$ (**Supplementary Figure S12**). Finally, by the 20th cycle (**Figure 3c**), the Ag-poor ORR profile with mass transport limited current density of ~ –1.5 mA cm_{geo}^{-2} has decayed, further resembling that of Mn. Similar to the pure Mn film, $Ag_{30}Mn_{70}$ exhibits low ORR performance likely because the near-surface is composed of almost entirely MnO_x (95% relative to the Ag-Mn content, **Figure 2e**). In contrast to the Mn and the Ag-poor samples, the final measured cycles of the Ag-rich (x = 70, 90, 95) thin films converge to approximately the same overall ORR CV profile (~0.86–0.87 V vs. RHE onset potential), with overall activities greater than that of Ag (**Figure 3c)**. Comparing the first (**Supplementary Figure S13**), best (**Figure 3b**), and last (**Figure 3c**) ORR CV cycles of the Ag_xMn_{1-x} thin films as illustrated in **Figure 3a**, we see that, despite variation in the absolute values of activity between cycles, the material composition-performance trends between the Ag-rich and poor motifs are consistent. Moreover, the distinct redox profiles of the Mn-rich and the Ag-rich samples, as shown in **Figure 3e** (see more details in **Supplementary Note S2** and **Supplementary Figure S14**), indicate intrinsically different Mn redox dynamics between the Mn-rich and Ag-rich motifs. The performance variation as a function of cycle could be due to non-trivial surface Mn redox dynamics/kinetics changing the active oxide species and/or Mn dissolution; these hypotheses will be analyzed further below.[18, 23, 24, 36]

To compare the average intrinsic (specific, AFM surface area weighted) activity trends of the Ag_xMn_{1-x} thin films, average kinetic current densities for the first (**Supplementary Figure 23**), best (**Figure 3b**), and last (**Figure 3c**) CVs, at least in triplicate, were calculated using the Koutecký–Levich equation and the surface area determined by AFM post-ORR testing (**Figure 3g** and **Supplementary Table S6**) and are shown in **Figure 3e** for the best (circles) and final

(triangles) cycle. For the best CVs specifically, the Ag-rich motif demonstrates kinetic current density enhancements at 0.8 V vs. RHE of 5–10× over that of pure Ag on average. $Ag_{95}Mn_5$ demonstrates the highest absolute activity and highest enhancement past pure Ag. Notably, for the last CV, which corresponds most closely to the post-ORR physical characterization shown in this work, the Ag-rich samples still demonstrate kinetic current density (or specific activity) enhancements up to 3× that of pure Ag at 0.8 V vs. RHE, and their activity profiles have largely stabilized and converged upon one another (**Figure 3c**). This dynamic activity and retained enhancement compared to Ag is also seen for a representative $Ag_{70}Mn_{30}$ thin film examined over 1000 ORR cycles at 500 mV s^{-1} and 1600 rpm (**Supplementary Figure S15**). For this film, the average (cathodic/anodic) onset potential (at –0.1 $mAcm_{geo}^{-2}$) increases from the initial 0.81 V (cycle 1) to 0.90 V by cycle 62 and then decreases only to 0.89 V vs. RHE by cycle 1000. With such clear and reproducible activity changes, investigating the material surface after electrochemical testing is necessary to develop a model of the active surface and build a fundamental understanding of material–activity relationships.

Post-ORR characterization via XAS (**Figure 2b**) and XPS (**Figure 2c–e** and **Supplementary Figure S1-S4,S10** and **Table S1**,**S5**) indicates that there is significant surface restructuring as seen by Mn-oxide species redox changes and/or Mn leaching as a function of cycling. We hypothesize that the surface restructuring forms similar active species on the surface *in situ* on all three Ag-rich Ag_xMn_{1-x} samples (x = 70, 90, 95) and is responsible for the activity convergence of the Ag-rich films. Specifically, for the Ag-rich samples, XPS quantification shows a decrease in Mn content in the near-surface of ~10–30 at% units after-ORR (**Figure 2d**,**e**). Similarly, the top ~20 nm region of the Ag-rich films also shows a depletion of Mn, suggesting that leached Mn was not replenished from below (**Figure 2d**). The $Ag_{30}Mn_{70}$ sample behaves quite differently; while no significant change in Mn near-surface XPS content is observed pre- vs. post-ORR, after ORR Mn enrichment is now observed deeper in the top ~20 nm region by XPS depth profiling (**Figure 2d**). In summary, all Ag-rich Ag-Mn samples demonstrate greater activity than pure Ag at the initial stages and improve even further upon cycling until all converge to a similar ORR CV profile, still with greater activity than Ag. This points to intriguing time dynamics at the surface of these active catalytic Ag-Mn materials.

Ex situ, HR XPS post-ORR (**Figure 2b** and **Supplementary Figure S1**,**S3**,**S4**,**S10** and **Table S1**,**S5**) suggests an overall increase in near-surface Mn oxidation state from the initial MnO-dominant nature to an oxidation state dominated by Mn_3O_4 ($Mn^{2/3+}$), Mn_2O_3 (Mn^{3+}), and/or MnO_2 (Mn^{4+}) species. The overall shapes[37] of the post-ORR Mn $L_{3,2}$ XANES (**Figure 2b**) of $Ag_{30}Mn_{70}$ and $Ag_{70}Mn_{30}$ also support XPS fitting and indicate that the dominant Mn oxidation state changes from Mn^{2+} to a higher valency ($Mn^{2+/3+}$, Mn^{3+} and/or Mn^{4+}) in both samples. The positive energy shift of ~0.5–2 eV in L_3 and L_2 whiteline positions (**Figure 2b**) is further evidence of the increase in Mn oxidation state after ORR testing. Despite Ag-Mn compositional and Mn valency changes, however, the Ag 3*d* XPS (**Supplementary Figure S1**) and Mn $L_{3,2}$ XANES (**Figure 2b** and **Supplementary Figure S9**) post-ORR still indicate that Ag and Mn are interacting electronically as shown by the negative BE shifts in the Ag 3*d* peaks and the $L_{3,2}$ peak area decrease with increased Ag content, respectively. Interestingly, while it is difficult to fully distinguish differences in the oxidation states of Mn in the post-ORR XPS and XAS, CV under N_2-saturation indicates distinct redox profiles of the Mn-rich and the Ag-rich samples suggesting intrinsically different redox dynamics (see extended N_2 CVs discussion in **Supplementary Figures 24** and **Supplementary Note S2**). Therefore, while surface sensitive *operando* characterization would be required to better understand the Mn-oxide redox dynamics during ORR and how they affect activity, our data supports the hypothesis that, in the near-surface of the mixed Ag_xMn_{1-x} films, Mn valency increases and Mn partially leaches. Accordingly, our results suggest that both the Mn content and valency play a role in tuning ORR activity.

Despite near-surface composition (**Figure 2e**) and Mn-valency (**Figure 2b**,**c**) changes, AFM (**Figure 3g**) indicates the surface remains quite flat. Elemental mapping from SEM-EDS (**Supplementary Figures S7**) and AES (**Figure 3h** and **Supplementary Figures S6**) suggests that overall Ag and Mn in the bulk and Ag and MnO_x in the near-surface, respectively, remained well-mixed throughout most of the near-surface within instrument resolution. **Figure 1** and **Table 1** summarize the physical characteristics of the films before and after ORR. As seen in **Figure 2f** and **2h** for representative $Ag_{90}Mn_{10}$, most of the near-surface of the Ag_xMn_{1-x} thin films remains well-mixed after ORR testing. Interestingly, however, AES (**Supplementary Figure S16**) suggests there are scarce places on the surface where MnO_x rich domains, on the scale of ~1 μm laterally, can be found after 20 cycles, which are likely very thin, as discussed below, given that

such features are not seen topographically in representative AFM imaging (**Supplementary Figure S8** and **Supplementary Table S4**). Furthermore, after the extended cycling (1000 CVs, 1 – 0 V vs. RHE at 500 mV s^{-1}) we see a similar performance trend as seen in **Figure 3a** despite an increase coverage of MnO_x-rich domains at the near-surface (see stability evaluation details in **Supplementary Figure S15**). We also observe the growth of smaller surface nano-island-like features on the mixed Ag-Mn and pure Mn films (unlike on Ag) (**Supplementary Figure S8** and **Supplementary Table S4**), seen by the bright circular features in AFM topography measurements (**Figure 3h**, **Supplementary Figure 8** and **Supplementary Table S4**). These features contribute to the RMSR of the films slightly up to 2 × increasing from ~5 nm (**Figure 2g**) to ~10 nm (**Figure 3g**). However, the surface topography remains on the nanometer scale demonstrating only small changes in total exposed catalyst surface area (<3%) (**Figure 2g**,**3g**, **Supplementary Figure 8** and **Supplementary Table S4**). Similarly, only a minor exposed surface area change (<5% increase in RF) is seen for the representative $Ag_{70}Mn_{30}$ film after 1000 ORR stability cycles (**Supplementary Figure S15**); however, surface nano-restructuring is more pronounced as shown by an increase in the number of these features seen by SEM and AFM. Given that these features are not observed on the pure Ag film, they could arise from partial MnO_x phase segregation at the surface during reaction (dissolved Mn is not expected to re-plate in the investigated potential range)[36]. Unfortunately, with AES elemental mapping, discussed in detail in **Supplementary Note S1**, we were not able to resolve the composition of the nano-island-like formations that are seen in the AFM. Any further surface physical restructuring owing to ORR testing would be very small and on length scales similar or lower than AFM resolution (e.g. <2 nm radially and ~1 Å vertically) and not compositionally resolvable with available techniques (which have tens of nanometers compositional resolution at best). Further below, we explore a different synthesis approach to create model Mn@Ag catalyst films, along with computational efforts, which together lead to improved understanding of catalytically relevant surface motifs involved in the Ag-Mn system.

CV cycling in N_2 offers a means for *in-situ* analysis of dynamic changes to the catalyst surface. Representative characteristic redox profiles before and after ORR for various representative Ag_xMn_{1-x} thin films are shown in **Supplementary Figure S14**. The plethora of Mn redox features (discussed in detail in **Supplementary Note S2**) in the investigated potential range makes double layer capacitance surface area probing inappropriate.[64] However, the fact that in the most

capacitive regions (e.g. ~0.43 V_{RHE}) of the characteristic profiles of the films before and after ORR are very similar (**Supplementary Figure S14**), further supports that the electrochemically available surface area does not significantly change after ORR testing. The small differences in the magnitudes of the redox features before and after ORR (**Supplementary Figure S14**) are likely due to the observed increased average Mn oxidation state and/or changes in the amount of Mn at the surface owing to Mn-leaching. Therefore, while the observed nano-island-like features may affect the composition and structure of individual surface active sites, as indicated by AFM and N_2-saturated cycling, any changes in average ORR performance across the samples are not likely due to surface roughening, but rather to intrinsic material property changes as a function of cycling that optimize the surface Ag-MnO_x composition and surface atomic/molecular arrangement.

In sum, for all the bulk Ag-rich samples, the Mn that moves to the surface oxidizes prior to electrochemical analysis and during ORR we see activity enhancements up to 10× compared to pure Ag, which allude to the presence of cooperative electronic interactions between surface Ag and MnO_x. The surface area of the films does not change substantially during operation, despite further surface oxidation, Mn dissolution, and possible MnO_x nano-island formation upon testing. This suggests that the activity of the system is sensitive to the Ag:MnO_x composition ratio and Mn-oxidation state, and could indicate that there are particular surface active sites formed *in situ*, that are common to the high performing samples. Tailored experimental approaches and density functional theory can help better understand the nature of active sites in the Ag-MnO_x surface electrocatalyst system.

3.2 Synthesis, Characterization, and ORR Activity Examination of Model Mn_y@Ag Thin Films

As discussed above, our Ag_xMn_{1-x} thin films have complex surfaces with interesting material dynamics during reaction. From a purely experimental point of view, and as discussed below in **Section 3.3** with DFT, various active site structures on Ag-MnO_x surfaces could result in sites with enhanced O-adsorption and thus ORR activity. Therefore, an experimental system with MnO_x only at the surface, as opposed to in the entire depth as in the Ag_xMn_{1-x} system, could provide further

insight into the nature of ORR catalysis on Ag-MnO_x. Specifically, such a system could help differentiate the ORR activity trends among various active site motifs (i.e. sites at or around Ag, MnO_x, and Ag–MnO_x surface interfaces). To experimentally study Ag-MnO_x surface structures in a more controlled configuration, we synthesized layered Mn_y@Ag_{70-y} thin films (Mn onto Ag), or Mn_y@Ag for short, where y = 0.3, 1, 5, and 10 nm (or 0.22, 0.72, 3.6, 7.2 μg_{Mn} cm_{geo}^{-2}), as measured *in situ* by QCMs during PVD (schematic of the system shown in **Figure 4**, structural and elemental imaging shown in **Supplementary Figure S6-S8**,**S17-S22,** see more details in **Supplementary Note S3**). Compared to the Ag_xMn_{1-x} thin films discussed above, the Mn_y@Ag thin film format allows for better control and understanding of surface structure and composition and can increase the apparent Mn surface sensitivity of physical characterization techniques that traditionally probe several nano- or micro-meters. Specifically, at low (sub-monolayer) Mn loadings/coverages, all Mn signal must come from the surface, since there is no thermodynamic driving force for Mn to migrate below the surface due to its oxophilicity (DFT-calculated segregation energies in **Supplementary Tables S2**,**S3**). We evaluated the electrochemical performance and the physical properties of the Mn_y@Ag thin films before and after electrochemical testing using similar methods to those discussed above (GI-XRD, SEM-EDS/AES, XPS, and CV under N_2- & O_2-saturation).

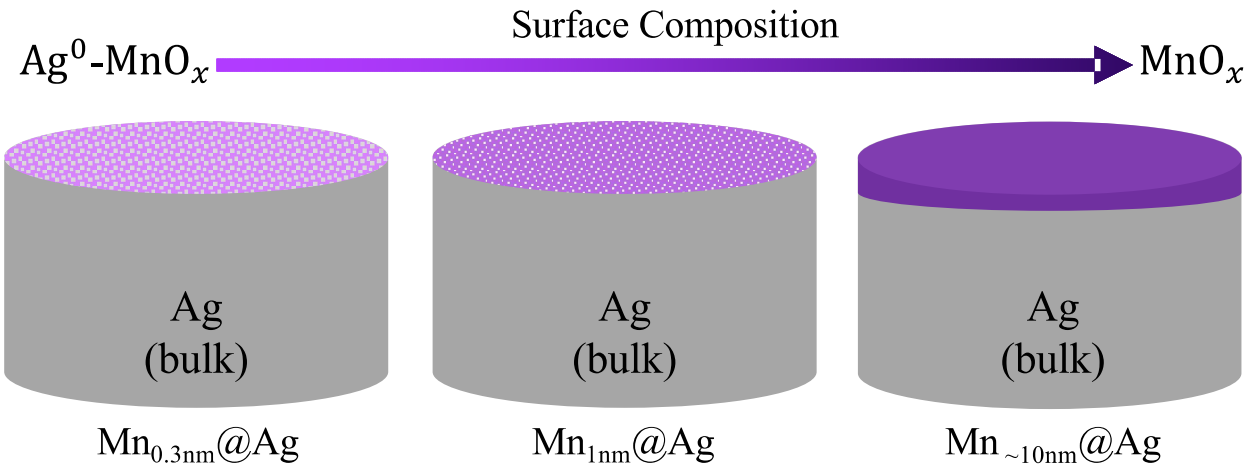

Figure 4. Schematic of representative sequentially-deposited Mn_y@Ag thin films illustrating a mixed Ag-MnO_x surface for y = 0.3 and 1 nm (or 0.22 and 0.72 μg_{Mn} cm_{geo}^{-2} respectively) and a fully MnO_x-coated surface for y = 10 nm. (or 7.2 μg_{Mn} cm_{geo}^{-2}).

In short, employing a set of combined extensive physical characterizing techniques, we observe, on average, the (air-exposed) Mn_y@Ag thin films are flat/smooth (AFM RFs ≤ 1.03 and RMSRs ≤ 5 nm; **Supplementary Figure S8** and **Table S4**), with Mn of dominant (~ >50%) Mn^{2+} character (HR Mn XPS in **Figure 5**, **Supplementary Figure S24** and **Table S7**) well-dispersed onto the Ag surface (AES elemental mapping in **Supplementary Figure S6**). From, XPS and AES we find that films likely range from partial Ag coverage ($Mn_{0.3nm}$@Ag and Mn_{1nm}@Ag) to full Ag coverage (i.e. Mn_{10nm}@Ag) as a function of deposition amount. Moreover, similar to the Ag_xMn_{1-x} thin films discussed above, we observe an increase in Mn oxidation state and partial Mn leaching after electrochemical testing (**Supplementary Table S7**). Structurally, as expected for such little deposited Mn, and similar to the GI-XRD results for the Ag_xMn_{1-x} thin films (except for x = 30), the diffractograms of all the Mn_y@Ag thin films (**Supplementary Figure S23**) are practically indistinguishable from that of pure Ag. **Figure 4** shows a qualitative sketch of the as-deposited Mn_y@Ag thin films' physical characteristics. Specific characterization of the (near-) surface of these films is detailed below.

The relative XPS Ag and Mn near-surface composition of the as-deposited films is shown in **Figure 5a**, verifying we indeed deposited Mn on the surface of the Ag thin films (see Survey and HR Ag 3*d* and Mn 2*p* XPS in **Supplementary Figure S2b**,**S24**, and tabulated results in **Supplementary Table S7**). Down to 0.3 nm of deposited-Mn, we see a Ag near-surface content of ~90 at% which decreases to ~50-60 at% with 1 nm of deposited-Mn. While XPS is not perfectly surface sensitive, this suggests that Mn likely does not fully coat the underlying Ag for y = 0.3 and 1 nm. Further corroboration is provided by representative low energy ion scattering spectroscopy (LEIS, **Supplementary Figure S25**), which truly probes the top-most atomic layer,[65] confirming that indeed at y = 0.3 nm there is still a substantial fraction of Ag atoms exposed at the top-most layer of the thin film, despite the deposition thickness being approximately equal to that of an atomic Mn metal monolayer. In contrast, the Ag near-surface content is ~0 at% at 5 nm and 10 nm of deposited Mn suggesting Mn likely initially covers/coats the entire underlying Ag thin film at these higher deposited-Mn thicknesses (**Figure 5a**) (a trace Ag 3*d* peak is identifiable in **Supplementary Figure S24a** for Mn_{5nm}@Ag suggesting that the underlying Ag is likely at about the XPS probe depth limit of a few nanometers).

In terms of oxidation state, as expected, no metallic Mn is seen in any of our XPS measurements (Su or HR) of the Mn_y@Ag system (**Supplementary Figure S2b**,**S24** and **Table S7**). This is in agreement with the results on Ag_xMn_{1-x} thin films (**Figure 2c** and **Supplementary Figure S3**), indicating that after air-exposure the Mn in the top 10-20 nm of the films is oxidized. HR Mn 2*p* (**Supplementary Figure S24**) and Mn 3*s* XPS (**Supplementary Tables S5**,**S7**) indicates that the oxidized Mn on the surface is predominantly Mn^{2+} (MnO) in character; also similar to the co-deposited films. Moreover, HR XPS follows the same trends seen for the Ag_xMn_{1-x} thin films, namely negative BE Ag 3*d* (**Supplementary Figure S24**) shifts upon surface electronic interactions with MnO_x and lack of distinguishable Mn 2*p* peak (**Supplementary Figure S24**) shifts due to Ag-mixing.

Altogether, the *ex situ* physical characterization (AFM, AES, XPS, and LEIS) of the Mn_y@Ag thin films suggest that this Mn_y@Ag sequential-deposition synthesis approach can produce well-dispersed MnO_x, with tunable coverage, on a Ag surface. In particular, the Mn_y@Ag thin films where Mn does not fully coats/covers the underlying Ag, namely y = 0.3 and 1 nm, could yield enhanced Ag–MnO_x surfaces with active sites motifs representative of those modeled by DFT, which we discuss further below in **Section 3.3**.

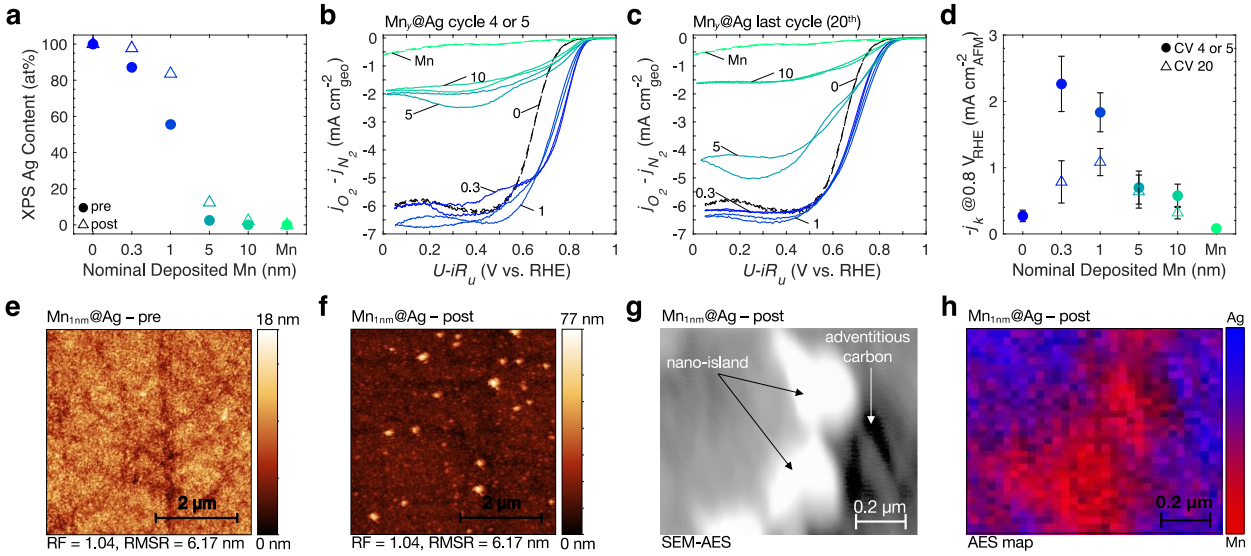

Figure 5. Representative electrochemical characterization of Mn_y@Ag thin films and post-testing composition. (**a**) Near-surface XPS compositional analysis before (circles) and after (triangles) ORR testing of Mn_y@Ag thin films. Representative ORR CV of Mn_y@Ag thin films comparing

the (**b**) 4th or 5th (best for y = 0.3, 1, 10 nm, 4th for y = 5 nm) and (**c**) last cycle. (**d**) Average kinetic current density at 0.8 V vs. RHE of Mn_y@Ag thin films comparing the 4th or 5th cycle (circles) and final (triangles) cycles normalized by post-ORR AFM roughness. Representative AFM topography imaging of Mn_{1nm}@Ag (**e**) before and (**f**) after 20 ORR cycles. (**g**) SEM image and corresponding (**h**) AES Ag/Mn elemental mapping of Mn_{1nm}@Ag post ORR testing at a nano-island feature (g and h were taken nominally at the same spot, although was some slight image drift during measurement). Note the black regions on **h** are from adventitious carbon contamination during measurement.

We evaluated the activity for the ORR activity of the layered, sequentially-evaporated, Mn_y@Ag thin films with the same electrochemical testing methods used for the co-deposited Ag_xMn_{1-x} thin films (see tabulated performance metrics in **Supplementary Table S6**). The ORR CV profiles for y = 5 and 10 nm (**Figure 5c**) show better performance than pure Mn, they do not however, reach the desired Ag-like, 4e^- selective, enhancement seen for y = 0.3 and 1 nm (or that of the Ag-rich Ag_xMn_{1-x} thin films). Given that the pure Mn thin film performs poorly for the ORR, this low performance is expected as XPS (**Figure 5a**) indicates that the near-surface (several nanometers) of the as-deposited y = 5 and 10 nm films is mainly composed of relatively thick MnO_x (98–100 at%). The minor performance improvement relative to pure Mn seen in **Figure 5c**,**d** could be due for instance to a different dominant exposed surface Mn oxidation state or structure during reaction, or improved oxide conductivity owing to the metallic Ag thin film support among other possibilities. In theory, the Ag substrate for the y = 5 and 10 nm films, and even for any thick/multilayer nano-islands on Ag, could possibly affect the activity of the top MnO_x film/sites. However, the overall poor ORR performance of the y = 5 and 10 nm films (**Figure 5b**) suggests that such substrate effects, across nanometers, are at most very minor.[66-69] The last ORR CV cycles shown in **Figure 5c** indicate that while the ORR CV performance improved for the y = 5 nm sample after 20 cycles, though without a significant change in specific activity (**Figure 5d**), the performance for y = 10 nm remained poor. As suggested by the XPS compositional (**Figure 5a**) analysis post-ORR testing discussed further below, this is likely due to sufficient Mn dissolution for y = 5 nm causing the exposure/creation of some Ag and/or cooperative Ag-MnO_x surface sites, which are hypothesized to be substantially more active than those of pure MnO_x, while there is insufficient dissolution for this to happen for the y = 10 nm thin film. Moreover, AFM measurements (**Figure 5e**,**f** and **Supplementary Figure S8** and **Table S4**) indicate that despite up

to 2 × RMSR increases compared to the as-deposited surfaces, changes in the total exposed surface area of the thin films are negligible.

Compared to the thicker Mn_y@Ag samples (y = 5 and 10 nm), the CV profiles and overall electrochemistry (CVs in O_2 and N_2) for y = 0.3 and 1 nm are very similar to each other, and demonstrate enhanced ORR activities relative to both parent materials, with up to ~ 50 mV greater onset potentials (**Figure 5b**) than pure Ag and specific activities 8× that of Ag at 0.8 V vs. RHE (**Figure 5d**). Additionally, similar to the Ag-rich Ag_xMn_{1-x} thin films after 20 cycles, and concomitant with partial Mn dissolution during reaction (**Figure 5a**), we observe (**Figure 5c**) that the ORR CVs for y = 0.3 and 1 nm converge to ~0.86–0.87 V_{RHE} average onset potential with average specific activities 3–4× that of pure Ag. The similarity of the ORR CVs between y = 0.3 and 1 nm (**Figure 5b**,**c**) supports the hypothesis that these two films likely have similar active sites structures. A mass activity analysis at 0.8 V vs. RHE (**Supplementary Table S8**) further suggests that active sites on the thin films with enhanced specific ORR activity can reach impressive ORR activities on both a Ag- and Mn-content bases. For instance, $Mn_{0.3nm}$@Ag demonstrates estimated average mass activities up to ~7 x10^3 mA $mg^{-1}_{Ag\ ML\ (\sim 0.3\ nm)}$ and ~10 × 10^3 mA mg^{-1}_{Mn}, assuming only a monolayer (ML) of Ag or all the Mn in the sample is active, respectively (**Supplementary Table S8**). Examining y = 0.3 nm specifically, the post-ORR Mn near-surface (XPS) composition is about 1 at% and despite this ultra-low Mn content, the final (20^{th}) ORR CV for this sample still demonstrates enhanced performance compared to pure Ag, suggesting that even small amounts of surface MnO_x can result in ORR specific activities 3× greater, on average, than that of Ag (**Figure 5a**,**c**,**d**). Such a Ag-rich surface, likely enabling dispersed cooperative Ag-MnO_x sites, with substantial average specific activity enhancements past Ag, supports the hypothesis that the observed ORR activity enhancements arise from electronic/ligand effects owing to the interactions between Ag and MnO_x. Ligand effects broadly refers to catalytically beneficial electronic interactions between surface sites and neighboring atoms; we discuss such effects with density functional theory in **Section 3.3**.

Further surface characterization of y = 0.3 and 1 nm post-ORR suggests that concomitant with Mn leaching during reaction, surface MnO_x phase-segregates into Mn-rich thin domains. Specifically,

AFM measurements (**Figure 5e**,**f** and **Supplementary Figure 8** and **Supplementary Table 4**) indicate the presence of nano-island-like features tens of nanometers tall (as opposed to the ultra-thin Ag-Mn mixed features on the as-deposited samples) that contribute negligibly to surface area. Interestingly, the as-deposited samples also have some evidence of periodically dispersed, ultra-thin (via AFM **Supplementary Figure 8),** bright round features (via SEM **Supplementary Figure S17-S19)** measuring ~50–200 nm in diameter. AES mapping (**Supplementary Figure S20**) indicates that these features could be initially homogeneous in Ag-Mn composition (see more details in **Supplementary Note S3**). AES near-surface mapping of nano-island-like features seen post-ORR, however, suggests these features become MnO_x rich (**Figure 5g**,**h** and **Supplementary Figure S21**). With AES (**Supplementary Figure S22)** we also see scarce laterally-larger, up to 1 μm laterally, MnO_x-rich domains. AES (**Supplementary Figure S6**,**S22)** also indicates that outside these MnO_x rich nano-islands the MnO_x remains nominally dispersed and not fully phase-segregated (within instrument resolution: tens of nanometers laterally) on the Ag surface, in agreement with the retention of Ag-Mn electronic structure hybridization on the near surface as demonstrated by the negative BE shifts in the Ag 3*d* XPS (**Supplementary Figure S24)**. Moreover, it is possible that there are smaller MnO_x nano-island regimes outside AES resolution.

As represented in **Figure 6a**, the N_2 CVs of the Mn_y@Ag thin films follow the trends seen on the Ag_xMn_{1-x} thin films where the samples that exhibit enhanced ORR performance (y = 0.3 and 1 nm; x = 70, 90, and 95; see the last CV representatively plotted together in **Figure 6b**) have similar characteristic CV profiles and redox features, distinct from the less-active samples with a greater/thicker Mn coverage, y = 5 and 10 nm (see all N_2 CVs in **Supplementary Figure S26**). For reference, a general representative qualitative illustration, from an experimental point of view, of the $Ag_{90}Mn_{10}$, Mn_{1nm}@Ag, and Mn_{10nm}@Ag thin films post-ORR evaluation is shown in **Figure 6c**. Interestingly, the plethora of Mn redox features common to the characteristic CVs of the Ag-rich samples **(Figure 6a**) for both the Mn_y@Ag and Ag_xMn_{1-x} thin films suggests that high amounts of surface Ag can stabilize the formation and presence of a variety of certain Mn-oxide species, concomitant with ORR activity enhancement. While the exact surface oxidation state changes are difficult to quantitatively describe without *operando* physical characterization, we hypothesize that the differences in redox behavior between the enhanced Ag-rich and the Mn-like samples' N_2

CV profiles are due to the presence of different dynamic oxide species at the surface, where certain species are preferentially stabilized by the presence of Ag compared to those present in the Mn-rich co-deposited and layered samples as well as the pure Mn sample.

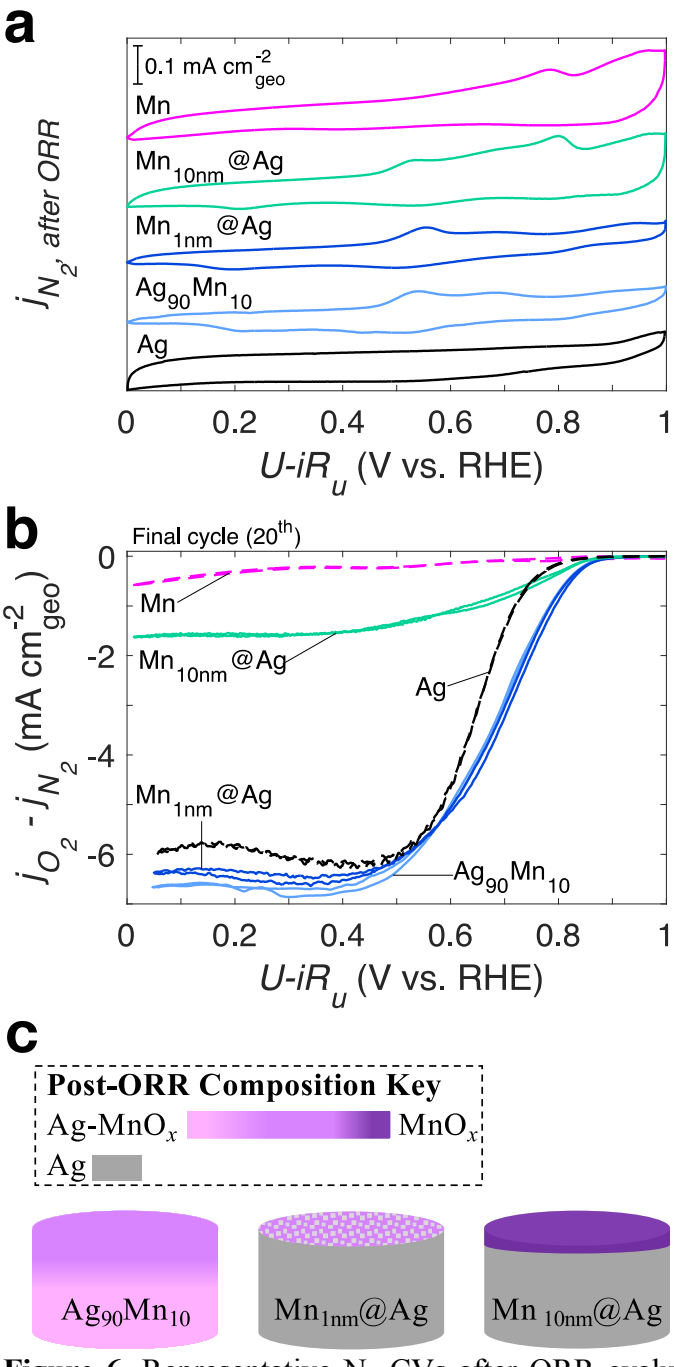

Figure 6. Representative N_2 CVs after ORR evaluation of select Mn_y@Ag and Ag_xMn_{1-x} thin films. Representative (**b**) last cycle ORR CVs comparing select Mn_y@Ag and Ag_xMn_{1-x} thin films (y = 1, 10 nm and x = 90). (**c**) Representative qualitative illustration, from an experimental

perspective, of the $Ag_{90}Mn_{10}$, Mn_{1nm}@Ag, and Mn_{10nm}@Ag thin films post-ORR evaluation (not to scale). The representative post-ORR near-surface XPS Ag-Mn composition is shown in **Figure 2e**,**5a**.

In **Sections 3.1** and **3.2** of this work, we gain insight on the average specific ORR activity trends on engineered Ag-MnO_x surfaces on Ag-Mn electrocatalysts. Comparing to previously reported representative catalyst performance (**Supplementary Table S9**), shows that on a geometric and mass loading bases (**Supplementary Tables S6**,**S8**,**S9**) our enhanced Ag-Mn thin films yield comparable or greater ORR performance than some Pt/C and Pd/C (powders/inks) catalysts. Moreover, comparing to previously studied representative Ag-Mn catalyst systems, for the most part on a geometric basis for nanoparticulate/ink-based catalysts (**Supplementary Tables S6**,**S8**,**S9**) demonstrates the activities of our enhanced Ag-Mn thin films to be among the highest reported. Notably, while we report specific activity, the specific catalyst surface area is often not well defined for nanoparticulate/powder/inks catalysts systems, thus making average intrinsic activity comparison difficult. Altogether, our experimental results demonstrate Ag-MnO_x surfaces as a robust catalyst motif with enhanced ORR activity owing to the cooperative interactions between metal and metal oxide.

3.3 DFT Modeling and Theoretical ORR Activity Evaluation of Ag-MnO_x Surface Structures

DFT calculations were performed to provide further understanding of the nature of the Ag-Mn surface under ORR conditions and elucidate possible active site motifs for the highly active Ag-rich catalysts described above. Consistent with previous studies,[53] we assumed a four-step ORR association reaction mechanism that proceeds through *OOH, *O, and *OH as reaction intermediates to evaluate theoretical ORR activity. Catalytic activities on various active site motifs are then calculated on the basis of the thermodynamic limiting potential for the ORR (U_L),[53] which is dependent on the surface binding energies of reacting oxygen intermediates (**see the Theory & Computational Methods section for details**). A more positive theoretical limiting potential (U_L) indicates a higher activity. In the context of DFT calculations, potentials are reported vs. the computational hydrogen electrode (CHE). It is important to note that while experimental-

theoretical activity trends can be compared, absolute theoretical activity metrics should not be compared directly with the experimentally measured current density-dependent ORR activities.[70]

As observed experimentally and discussed in the previous sections, the surface and the near-surface regions of the Ag_xMn_{1-x} thin films are enriched with Mn in an oxidized state relative to the bulk metallic Mn content owing to Mn migration and oxidation upon air-exposure (**Figure 2a-c** and **Supplementary Figures S1**,**S3**,**S4**,**S10** and **Table S1**,**S5**). Moreover, in addition to partial Mn leaching during testing (**Figure 2d,e**), the Mn valency is observed to increase after ORR catalysis (**Figure 2b,c**). We computationally evaluate Mn migration by calculating segregation energies for a bulk Mn atom to move to the surface in a metallic Ag_xMn_{1-x} unit cell under vacuum and in the presence of adsorbed *O and *OH intermediates. Segregation of a bulk Mn atom to the surface of a metallic Ag_xMn_{1-x} unit cell is calculated to be unfavorable under vacuum conditions, while, in the presence of adsorbed *OH, and *O, segregation becomes thermodynamically favorable (see **Supplementary Table S2)**. We further evaluated segregation energies under dilute conditions of Mn in a Ag(111) unit cell and observed a similar trend (**Supplementary Table S3**). This suggests that in air and under ORR conditions, the surface thermodynamically favors Mn enrichment and oxidation in agreement with our experimental observations.

The complex Ag-Mn oxide surface of our thin films could exhibit a plethora of active site configurations including pure Ag sites, pure MnO_x sites, Ag–MnO_x interfacial sites of different forms, and pure Ag or MnO_x sites neighboring Ag–MnO_x interface sites. Coupled with our experimental methods, DFT helps us gain insight into likely surface active site motifs responsible for the experimentally observed activity trends. Initially, a single Mn metal atom trapped in a Ag(111) surface (**Supplementary Table S10)** was modeled, and even with increased O-coverage on the Mn atom, DFT calculations show poor ORR limiting potentials $\leq$ –0.18 V at the Mn_{atom}–Ag bridge site, indicating that atomic metal Mn sites trapped within the Ag lattice are unlikely to account for the activity enhancements seen electrochemically. We did not perform ORR activity calculations on metallic Ag_xMn_{1-x} unit cells since on these mixed metallic Ag-Mn surfaces, bulk Mn atoms segregate to the surface and surface Mn atoms undergo oxidation under the ORR reaction conditions (**Supplementary Table S2**). Surface MnO_x nanostructures, however, could potentially form and play a role in catalysis, given their thermodynamic favorability as shown

computationally (see below) and the Mn surface segregation and oxidation observed experimentally (described above). Therefore, to model our Ag-Mn catalysts we also investigated possible Ag-MnO_x surface motifs by examining a variety of surface nano-scale structures such as nano-stripes and nano-islands on Ag(111) that could thermodynamically arise during the ORR. **Figure 7** shows DFT calculations of representative nanostructures on Ag(111) in addition to bulk manganese oxides for comparison. For these calculations, we selected Mn_2O_3 and Mn_3O_4 bulk structures, consistent with those thermodynamically expected in the kinetic and mixed kinetic-diffusion limited ORR region seen on our thin films (~0.6–1 V_{RHE}),[6, 36] with Pbca [61] and I41/amd [141] space groups, respectively. The optimized bulk structures were then used to generate the surface structures that fulfill their respective stoichiometries, and the one with lowest surface energy was selected for activity calculations following the theoretical framework developed in a previous study.[54] The Mn_2O_3(100) and Mn_2O_3(110) surfaces (**Figure 7a**) demonstrate a U_L of 0.71 V and 0.73 (**Figure 7b**), whereas the U_L of the Mn_3O_4(001) surface is 0.69 V,[71] in agreement previously reported[59] theoretical ORR activities. Interestingly, while higher valent (> 2+) Mn-oxides are well known alkaline ORR electrocatalysts[30, 32-34, 59, 60] and outperform the DFT-calculated activity of the pure Ag(111) surface which has a U_L of 0.61 V (**Figure 7b**),[8] Mn(II)O is known to be rather inactive[30] for the ORR. While there are several ORR-active bulk Mn-oxides,[30, 33, 34, 59, 60] we further investigated possible motifs of the Ag-MnO_x surface by examining a variety of surface nano-scale structures such as nano-stripes and nano-islands that may arise during ORR and contribute to catalytic activity.

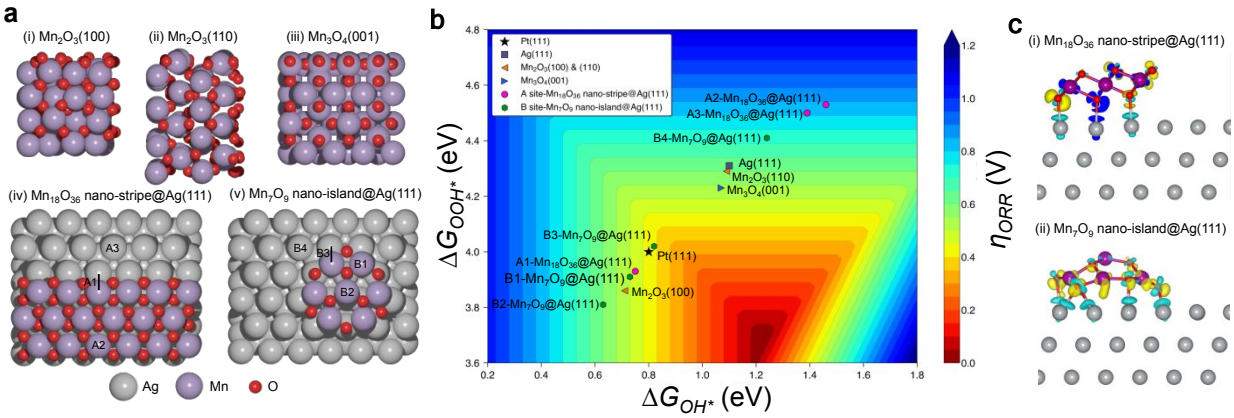

Figure 7. DFT-calculated ORR activity on Ag-MnO_x active site motifs. (a) Ag-MnO_x active site models investigated by DFT for their effect on ORR activity: (i) Mn_2O_3(100), (ii) Mn_2O_3(110),

(iii) Mn_3O_4(001), (iv) $Mn_{18}O_{36}$ nano-stripe@Ag(111), and (v) Mn_7O_9 nano-island@Ag(111). (**b)** ORR activity map showing overpotentials (vs. CHE) for various Ag-MnO_x structures calculated by DFT. $\eta = 1.23\ V - U_L$. (The ORR U_L is defined as the highest potential at which all the reaction steps become downhill in energy. Lower η or higher U_L indicate improved theoretical ORR activity). (**c)** Side-view of charge density plots indicating regions with depleted electron density in teal and excess electron density in yellow colors (isosurface levels plotted from −0.0004 to +0.0004 e $bohr^{-3}$).

The tabulated thermodynamic stability and theoretical ORR activity on various MnO_x nanostructures on Ag(111) is summarized in **Supplementary Table S11**. The ORR limiting potential for a number of different active sites on MnO_x nanostructures@Ag(111), as well as for pure Ag, and pure Mn oxides is shown in **Figure 7b**. In short, our computational study demonstrates that several Ag–MnO_x interface site configurations can lead to substantially improved ORR activity relative to on Ag(111) despite the possibility for other less enhanced sites.

We modeled a broad range of thermodynamically stable MnO_x nanostructures@Ag(111) (**Supplementary Table S11**). The first nano-scale structure that we considered was a single layer $Mn_{18}O_{36}$ nano-stripe on a Ag(111) surface (**Figure 7a**.**iv**). We selected three oxide units separated by three Ag metal rows and the calculated lattice constants are within 5% of each other.[72] The $Mn_{18}O_{36}$ nano-stripe bonds to the Ag(111) surface via oxygen atoms and the calculated formation energy for $Mn_{18}O_{36}$ nano-stripe@Ag(111) is –0.08 eV per Mn atom indicating these nano-stripes are relatively stable on the Ag(111) surface (**Supplementary Table S11**). The $Mn_{18}O_{36}$ nano-stripe features two types of edge sites (**Figure 7a**.**iv**), a Ag–MnO_x interface site (A1) where a large synergistic interfacial effect is expected and a top Mn edge site (A2). Interestingly, compared to Ag(111) with a U_L of 0.61 V, the A1 site has a an enhanced U_L of 0.75 V (**Figure 7b**) and increasing the *OH coverage at the Ag-Mn interface sites to 1 ML results in a U_L of 0.72 V (**Supplementary Table S12**). In contrast, *OH adsorbs weakly on the Mn top site (A2) with a U_L of 0.42 V (**Figure 7b**). The Ag atoms at the vicinity of $Mn_{18}O_{36}$ nano-stripe (A3) have a decreased activity, with a 0.39 V U_L due to the charge transfer from Ag atoms at the vicinity of the $Mn_{18}O_{36}$ nano-stripe to the $Mn_{18}O_{36}$ nano-stripe (**Figure 7b**). To understand the electronic interactions between the $Mn_{18}O_{36}$ nano-stripe and the Ag(111) surface, we conducted a Bader charge analysis and computed the isostructural charge density differences (**Figure 7c**, **Supplementary Table**

S13). We calculate a 0.28 *e* per MnO_2 charge transfer from Ag(111) to the $Mn_{18}O_{36}$ nano-stripes and visualization of charge transfer further demonstrates that oxygen and Mn atoms of the nano-stripes gain electrons from Ag(111).[72]

The second nano-scale structure that we considered was Mn_7O_9 nano-islands on a Ag(111) surface (**Figure 7a**). We sampled a selected number of other single layer MnO_x nano-islands on a Ag(111) surface and among the considered nano-islands structures, Mn_7O_9 nano-islands@Ag(111) was found to be the most stable structure with a formation energy –0.75 eV per Mn atom (**Supplementary Figure S8**). Unlike the $Mn_{18}O_{36}$ nano-stripe which bonds to the Ag(111) surface through O atoms, MnO_x nano-islands bond to the surface through Mn atoms. This results in non-stoichiometric Mn:O for MnO_x surface nano-islands compared to the bulk Mn-oxides. The Mn_7O_9 nano-islands@Ag(111) possess multiple active site motifs: top Mn edge site (B1), Mn center site (B2), Ag–MnO_x interface site (B3), and the Ag atoms neighboring to the Mn_7O_9 nano-island (B4) (**Figure 4a**). As shown in **Figure 4b**, the B1 and B2 sites, where ORR intermediates adsorb on top of a Mn atom, demonstrate, respectively, a U_L of 0.73 V (greater than for Ag(111)) and 0.63 V (comparable to Ag(111)). This indicates that sites analogous to B1 (**Figure 7a**), namely top Mn edge sites at Ag-MnO_x interfaces of certain structures, could be partly responsible for the experimentally observed enhanced activity on our Ag-rich thin films. Meanwhile, sites similar to B2, possibly demonstrating beneficial substrate or subsurface ligands effects, likely would have a neutral effect on ORR activity as they would be indistinguishable from Ag in terms of theoretical activity (**Figure 7a**,**b**). As demonstrated in **Supplementary Table S11**, the geometry of the MnO_x nanostructures@Ag(111) affects the theoretical ORR activity of the possible surface active sites. For instance, unlike for the Mn_7O_9 nano-island where we find the top Mn edge site yields enhanced ORR activity, for the Mn_6O_7 nano-island (**Supplementary Table S11**) we find such sites to have a poor activity (U_L of 0.14 and 0.07 V for Mn top sites S1 and S2), with the only differences between the structures being their shape and stoichiometry (as noted above, the Mn top site of the MnO_x nano-stripe@Ag(111) also yields poor theoretical ORR activity).

Remarkably, the Ag–MnO_x interface site (B3) on the Mn_7O_9 nano-island has a U_L of 0.81 V (**Figure 7b**), significantly greater than that of Ag(111) and comparable to that of Pt(111) and Pd(111),[8] demonstrating the possible synergistic ligand effects on ORR activity at Ag–MnO_x

interface sites. Similarly, we find the Ag–MnO_x interface active site on the Mn_6O_7 nano-island (**Supplementary Table S11**) also has a substantially enhanced theoretical ORR activity with a U_L of 0.79 V. In contrast, the Ag atoms at the vicinity of Mn_7O_9 nano-island (B4) experience a detrimental electronic effect with a decreased U_L of 0.45 V (**Figure 4b**), and we see similar results on the other MnO_x nano-islands (**Supplementary Table S11**) we investigated. Similar to the $Mn_{18}O_{36}$ nano-stripe@Ag(111) system, we observed that Ag(111) donates electrons to the Mn_7O_9 nano-islands (0.13 *e* per $MnO_{9/7}$) but to a lesser extent (**Figure 4c**, **Supplementary Table S13**).

Ultimately, our DFT calculations on various thermodynamically stable MnO_x nano-structures@Ag(111) suggest that certain MnO_x structures on Ag can yield electronically enhanced ORR active sites. Moreover, our calculations suggest that the robust Ag–MnO_x interface active site motif could be the main contributor to the synergistic ORR activity enhancement seen for the Ag-rich Ag_xMn_{1-x} relative to pure Ag or Mn (MnO_x). Another active site motif that could play a role in the experimentally observed activity enhancements is the top Mn site at the Ag–MnO_x interface; however, the theoretical activity of this motif is highly dependent on MnO_x geometry and stoichiometry. This theoretical study further illustrates that despite changes in geometry and stoichiometry, Ag-MnO_x surfaces can provide active sites with tuned ORR activity, substantially improved compared to bulk Mn-oxides and pure Ag.

To assess how the valence electronic structure of a representative MnO_x nanostructure@Ag(111) compares to the that experimentally measured on our Ag_xMn_{1-x} and Mn_y@Ag thin films and to gain further insight into the surface bonding environment we employed combined valence band (VB) XPS and DFT projected-density of states (PDOS) modeling. **Figure 8a-c** demonstrates similar VB shape and center trends as a function of near-surface composition between Ag_xMn_{1-x} and Mn_y@Ag (see more VB details in **Supplementary Figure S10** and **Table S5**). Specifically, as seen in **Figure 8a-c,** the VB center systematically shifts to lower BEs with increasing Mn content, from 6.0 eV for pure Ag metal to 3.9 eV for the pure Mn thin film. The VB for Ag and Mn shown in **Figure 8a-c** are consistent with those previously reported for Ag[44, 73-75] metal and MnO[43], in agreement with the x-ray spectroscopic analysis employed in this work and discussed above. Moreover, the Ag-rich thin films (x = 95, 90, 70 % and y = 0.3 and 1 nm) exhibit a VB shape similar to that of pure Ag, while the Mn-rich thin films (x = 30 % and y = 5 and 10 nm)

exhibit a VB shape closer to that of the pure Mn thin film. Given that the VB probes the electrons involved in bonding, including those in the *d*-band,[43, 44, 73-75] trends in VB center and/or normalized area could relate to changes in average near-surface adsorbate binding strength.[76] Therefore, if the *d*-band of the Ag_xMn_{1-x} and Mn_y@Ag thin films followed the VB trends shown in **Figure 8a-c** as a function of Ag-Mn composition, according to the *d*-band center model[77] this could suggests that adsorbate binding strength of the Ag-Mn thin films increases with increasing Mn content. Moreover, **Figure 8d** shows DFT calculated PDOS of Mn (across all Mn atoms) on MnO and Mn_7O_9 nano-island@Ag(111) (a representative MnO_x nanostructure@Ag(111) with enhanced sites), while **Figure 8e** illustrates the DFT calculated PDOS of a Ag on a Ag(111) surface and interface Ag (site B3) on Mn_7O_9 nano-island@Ag(111). Mn in MnO (**Figure 8d.i**) has a higher *d*-band compared to metallic Ag (**Figure 8e.i**) suggesting Mn could adsorb ORR intermediates more strongly. Interestingly, the *d*-band of Mn (projected across all Mn atoms) in Mn_7O_9 nano-island@Ag(111) is slightly lower compared to Mn in MnO indicating a weaker oxygen adsorption on Mn atoms which results in increased theoretical activity.[76] Moreover, the Ag-projected PDOS at interface Ag (site B3) on the Mn_7O_9 nano-island@Ag(111) demonstrates a *d*-band upshift, indicative of increased adsorption strength, relative to Ag(111), as well as an overall similar shape to both the Ag-projected PDOS of Ag(111) and the VB for the Ag_xMn_{1-x} and Mn_y@Ag thin films where x = 95, 90, 70 % and y = 0.3 and 1 nm. Together, the Ag- and Mn-projected PDOS demonstrate an enhanced *d*-band electronic structure,[76] arising from the interactions between Ag and MnO_x, (the theorical activity at each possible active site is discussed in above and reported in **Supplementary Table S11**). These valence, and more importantly *d*-band, electronic structure changes have important implications in ORR electrocatalysis as Ag is known to bind O-based reaction intermediates weaker than would an optimal ORR catalyst.[8, 53] Therefore increasing adsorbate binding strength of Ag-based active sites (e.g. Ag–MnO_x interface sites) could result in enhanced ORR catalysis as demonstrated experimentally (**Figure 3** and **Figure 5**) and theoretically (**Figure 7**) in this work.[78] However, as demonstrated by the poor ORR performance of the of $Ag_{30}Mn_{70}$ and Mn thin films described earlier (**Figure 3b-d**,**f**), **Figure 8** could suggest that too much MnO_x content may instead result in too strong adsorbate binding. Together VB XPS and DFT PDOS analysis suggest that MnO_x nano-islands/structures@Ag(111) are a reasonable model to investigate theoretical ORR activity of the Ag-MnO_x surfaces on our thin films and further

elucidates the need for sufficient surface Ag content to tune O-adsorption and thus enhance ORR activity.

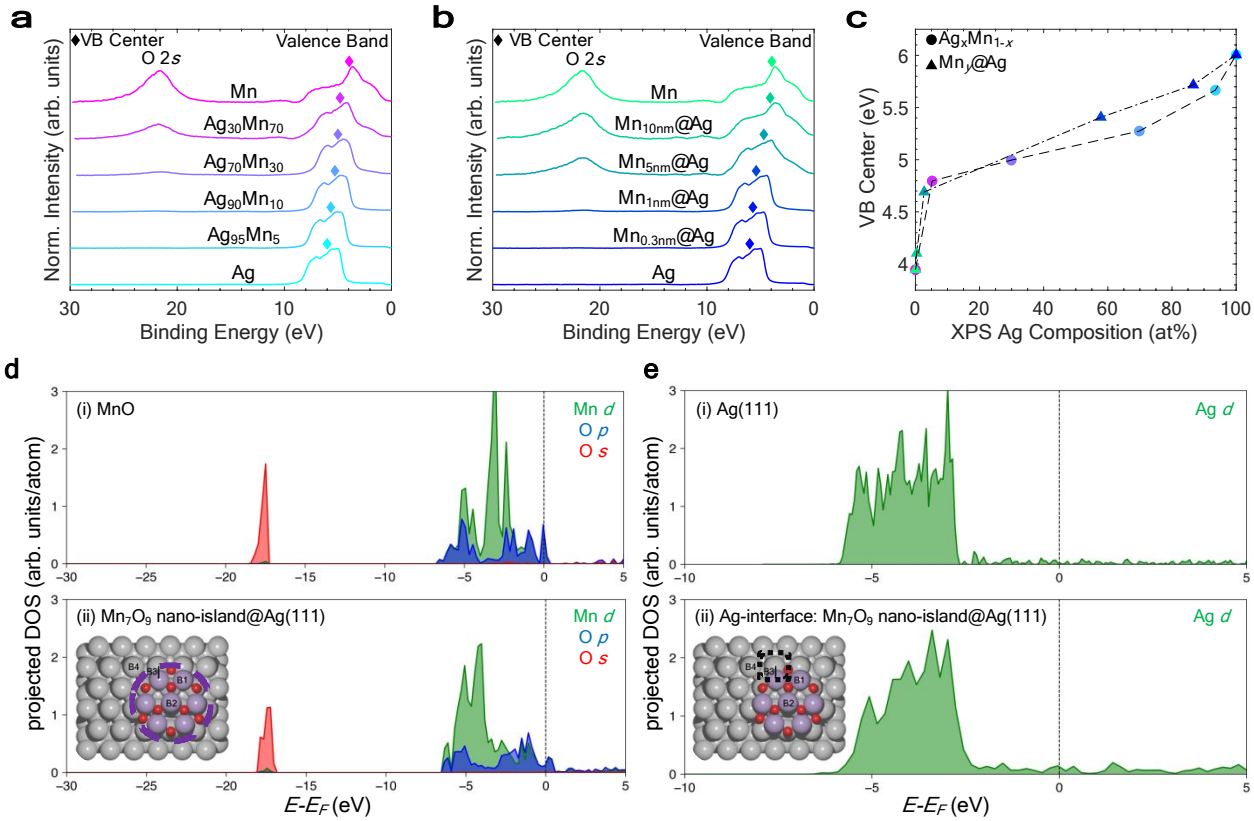

Figure 8. Ag-Mn VB XPS and DFT-calculated DOS. Representative valence band (VB) XPS after Ar^+ sputtering cleaning of the as-deposited (air-exposed) (**a**) Ag_xMn_{1-x} and (**b**) Mn_y@Ag thin films with their corresponding (**c**) VB-center (VB weighted/integrated mean energy) as a function of XPS Ag content (also shown in **a**,**b** as diamonds). (**d**) Mn-Projected (all Mn atoms) density of states (PDOS) for (i) MnO and (ii) Mn_7O_9 nano-island@Ag(111), and (**e**) Ag-Projected DOS (i) for a surface atom on Ag(111) and (ii) for the B3 site (Ag-interface) on Mn_7O_9 nano-island@Ag(111).

Together, DFT and electrochemical and physical characterization of both the Ag_xMn_{1-x} and Mn_y@Ag thin films support the hypothesis that Ag-MnO_x surfaces can have intrinsically enhanced activity for the ORR owing to the tuned oxygen adsorption energy induced by the optimal hybridization of the local electronic structures of surface Ag and MnO_x. While DFT highlights Ag–MnO_x interface sites as the most promising active site motif, this does not discount the presence of other possible active sites; however, it points us towards promising motifs with demonstrated activity and resiliency.

4. CONCLUSION

Ag-Mn electrocatalysts were synthesized by PVD co-deposition, forming well-mixed Ag-MnO_x surfaces that were studied extensively by experimental and computational methods probing material thermodynamics, composition, topography, electronic structure, and electrochemical behavior for the ORR. These co-deposited catalyst materials, irrespective of Ag-Mn nominal composition, formed similar Ag-MnO_x surfaces on a metallic Ag-Mn bulk. Ag_xMn_{1-x} thin films with sufficiently high Ag content at the surface yielded enhanced specific ORR activity up to 10 $\times$ that of pure Ag at 0.8 V vs. RHE. Among various possible active sites, DFT calculations demonstrate that certain Ag–MnO_x interface site configurations exhibit highly optimized oxygen binding across various geometries and stoichiometries, a plausible basis for the observed ORR activity. Motivated by the theorized active surface structure and to improve our control over the active catalyst surface, a parallel synthesis approach was employed to achieve Ag-MnO_x surfaces by sequential deposition of Mn thin films in the range of 0.3 – 10 nm cm_{geo}^{-2} onto Ag thin films (Mn@Ag). The sequentially deposited system was also highly catalytically active when sufficient surface Ag was exposed to enable synergistic surface electronic interactions between Ag and MnO_x, demonstrating specific activity enhancements up to 8-fold over pure Ag at 0.8 V vs. RHE. Altogether, this work supports the hypothesis that Ag–MnO_x surfaces can have intrinsically enhanced activity for the ORR owing to the tuned optimal hybridization of the electronic structures of surface Ag and MnO_x. Our work probing the origin of Ag-MnO_x activity enhancements for the ORR in alkaline conditions highlights the interplay between active site electronic structure, geometry, and catalytic performance and is translatable across a diverse range of electrochemical conditions (e.g. acidic electrolytes, fuel cells, electrolyzers, metal-air batteries). Furthermore, the identification of the Ag–MnO_x interface site, via DFT, as a promising active site motif motivates further experimental development and investigation of other enhanced metal-metal oxide electrocatalysts.

Cyclic voltammetry in N_2 and *ex situ* x-ray spectroscopies reveal that a plethora of MnO_x species may be present at the surface during reaction, with the thin films yielding enhanced ORR activity

having similar redox features and suggesting that certain desirable (for improved ORR) Mn-oxide species may be stabilized/promoted by Ag. These findings have broad implications in the fields of energy, environment, chemistry, and chemical-biology for applications, particularly in cases where stabilizing a particular, perhaps nominally unattainable, phase of a material (e.g. a certain type of Mn-oxide) is desired under certain operating conditions. We provide fundamental insight on the nature of ORR activity enhancements on Ag-Mn systems and on how to further engineer material systems with enhanced active sites. This work further provides a platform to fundamentally investigate material-property relationships of complex metal-metal oxide electrocatalytic surfaces, which can be used to engineer active sites with tuned electronic structures. Through improved electrocatalyst design, development, and fundamental understating of intrinsic material-property relationships, renewable electrochemical energy conversion technologies have an opportunity to greatly benefit the environment and humankind, mitigating anthropogenic climate change.

AUTHOR INFORMATION

Corresponding Author

* mburkes@stanford.edu. * jaramillo@stanford.edu.

Present Addresses

† Materials Science Division, Lawrence Livermore National Laboratory, Livermore, California 94551, United States.

Author Contributions

The manuscript was written through contributions of all authors. All authors have given approval to the final version of the manuscript. Conceptualization by J.A.Z.Z., G.T.K.K.G., M.B.S.; methodology by J.A.Z.Z. (PVD, CV, GI-XRD, XPS, AFM, SEM-EDS, AES), G.T.K.K.G.

(theory/DFT), M.B-N. (AES, SEM-EDS), M.A.H. (XAS), and J.E.A.A. (SEM); data curation by J.A.Z.Z. (PVD, CV, GI-XRD, XPS, AFM, SEM-EDS, AES, XAS, LEIS), G.T.K.K.G. (theory/DFT), G.A.K. (XPS), M.B-N. (AES, SEM-EDS), M.A.H. (XAS), and J.E.A.A. (SEM); data analysis and validation by J.A.Z.Z., M.B.S., G.T.K.K.G., M.E.K., G.A.K., M.B-N., M.A.H., J.E.A.A., J.K.N., and T.F.J.; writing—original draft by J.A.Z.Z., G.T.K.K.G., and M.B.S.; writing—review & editing by J.A.Z.Z., G.T.K.K.G., M.B.S., M.E.K., M.B-N., G.A.K., M.A.H., J.E.A.A., J.K.N., and T.F.J.; funding acquisition by J.K.N. and T.F.J.; supervision and project administration by M.B.S., J.K.N., and T.F.J.

Funding Sources

This work was supported by the Toyota Research Institute. Some of the research efforts involving thin film synthesis and XAS characterization were supported by the U.S. Department of Energy, Office of Science, Office of Basic Energy Sciences, Chemical Sciences, Geosciences, and Biosciences Division, Catalysis Science Program to the SUNCAT Center for Interface Science and Catalysis. Part of this work was performed at the Stanford Nano Shared Facilities (SNSF), supported by the National Science Foundation under Award ECCS-2026822. Use of the Stanford Synchrotron Radiation Lightsource (SSRL) at SLAC National Accelerator Laboratory is supported by the U.S. Department of Energy, Office of Science, Office of Basic Energy Science, under Contract DE-AC02-76SF00515. Work at the Molecular Foundry was supported by the Office of Science, Office of Basic Energy Sciences, of the U.S. Department of Energy under Contract No. DE-AC02-05CH11231. J.A.Z.Z. gratefully acknowledges support of the Gates Millennium Graduate Fellowship/Scholarship. G.A.K. gratefully acknowledges support from the National Science Foundation Graduate Research Fellowship under Grant No. 1650114.

Conflicts of interest

There are no conflicts to declare.

ACKNOWLEDGMENTS

This work was supported by the Toyota Research Institute. Some of the research efforts involving thin film synthesis and XAS characterization were supported by the U.S. Department of Energy, Office of Science, Office of Basic Energy Sciences, Chemical Sciences, Geosciences, and Biosciences Division, Catalysis Science Program to the SUNCAT Center for Interface Science and Catalysis. Part of this work was performed at the Stanford Nano Shared Facilities (SNSF), supported by the National Science Foundation under Award ECCS-2026822. Work was performed in part in the nano@Stanford labs, which are supported by the National Science Foundation as part of the National Nanotechnology Coordinated Infrastructure under award ECCS-1542152. Use of the Stanford Synchrotron Radiation Lightsource (SSRL) at SLAC National Accelerator Laboratory is supported by the U.S. Department of Energy, Office of Science, Office of Basic Energy Science, under Contract DE-AC02-76SF00515. Work at the Molecular Foundry was supported by the Office of Science, Office of Basic Energy Sciences, of the U.S. Department of Energy under Contract No. DE-AC02-05CH11231. We thank Dr. Joel Sanchez, Dr. Alessandro Gallo, and Molecular Foundry scientist Dr. Virginia Altoe for valuable discussions. We thank SSRL scientist Dr. Dennis Nordlund for his assistance in setting up and operating beam line 8-2. J.A.Z.Z. gratefully acknowledges support of the Gates Millennium Graduate

Fellowship/Scholarship. G.A.K. gratefully acknowledges support from the National Science Foundation Graduate Research Fellowship under Grant No. 1650114.

REFERENCES

1. S. R. Dhanushkodi, N. Mahinpey, A. Srinivasan and M. Wilson, *J. Environ. Inform.*, 2008, **11**, 36-44.
2. I. Staffell, D. Scamman, A. Velazquez Abad, P. Balcombe, P. E. Dodds, P. Ekins, N. Shah and K. R. Ward, *Energy Environ. Sci.*, 2019, **12**, 463-491.
3. D. R. Dekel, *J. Power Sources*, 2018, **375**, 158-169.
4. X. X. Wang, M. T. Swihart and G. Wu, *Nat. Catal.*, 2019, **2**, 578-589.
5. H. A. Hansen, J. Rossmeisl and J. K. Nørskov, *Phys. Chem. Chem. Phys.*, 2008, **10**, 3722-3730.
6. M. Pourbaix, *Atlas of electrochemical equilibria in aqueous solutions*, National Association of Corrosion Engineers, Houston, TX, Second Eng edn., 1974.
7. R. C. Sekol, X. Li, P. Cohen, G. Doubek, M. Carmo and A. D. Taylor, *Appl. Catal., B: Environ.*, 2013, **138-139**, 285-293.
8. J. A. Zamora Zeledón, M. B. Stevens, G. T. K. K. Gunasooriya, A. Gallo, A. T. Landers, M. E. Kreider, C. Hahn, J. K. Nørskov and T. F. Jaramillo, *Nat. Commun.*, 2021, **12 (620)**, 1-9.
9. D. A. Slanac, W. G. Hardin, K. P. Johnston and K. J. Stevenson, *J. Am. Chem. Soc.*, 2012, **134**, 9812-9819.
10. L. E. Betancourt, A. Rojas-Pérez, I. Orozco, A. I. Frenkel, Y. Li, K. Sasaki, S. D. Senanayake and C. R. Cabrera, *ACS Appl. Energy Mater.*, 2020, **3**, 2342-2349.
11. W.-B. Luo, X.-W. Gao, S.-L. Chou, J.-Z. Wang and H.-K. Liu, *Adv. Mater.*, 2015, **27**, 6862-6869.
12. Y. Wang, Y. Liu, X. Lu, Z. Li, H. Zhang, X. Cui, Y. Zhang, F. Shi and Y. Deng, *Electrochem. Commun.*, 2012, **20**, 171-174.
13. B. M. Gibbons, M. Wette, M. B. Stevens, R. C. Davis, S. Siahrostami, M. Kreider, A. Mehta, D. C. Higgins, B. M. Clemens and T. F. Jaramillo, *Chem. Mater.*, 2020, **35**, 1819–1827.

14. D. Higgins, M. Wette, B. M. Gibbons, S. Siahrostami, C. Hahn, M. Escudero-Escribano, M. García-Melchor, Z. Ulissi, R. C. Davis, A. Mehta, B. M. Clemens, J. K. Nørskov and T. F. Jaramillo, *ACS Appl. Energy Mater.*, 2018, **1**, 1990-1999.
15. Y. Lu, N. Zhang, L. An, X. Li and D. Xia, *J. Power Sources*, 2013, **240**, 606-611.
16. A. Holewinski, J.-C. Idrobo and S. Linic, *Nat. Chem.*, 2014, **6**, 828-834.
17. D. A. Slanac, A. Lie, J. A. Paulson, K. J. Stevenson and K. P. Johnston, *J. Phys. Chem. C*, 2012, **116**, 11032-11039.
18. S. A. Park, H. Lim and Y. T. Kim, *ACS Catal.*, 2015, **5**, 3995-4002.
19. Q. Wu, L. Jiang, L. Qi, L. Yuan, E. Wang and G. Sun, *Electrochim. Acta*, 2014, **123**, 167-175.
20. S. Sun, H. Miao, Y. Xue, Q. Wang, S. Li and Z. Liu, *Electrochim. Acta*, 2016, **214**, 49-55.
21. F. W. T. Goh, Z. Liu, X. Ge, Y. Zong, G. Du and T. S. A. Hor, *Electrochim. Acta*, 2013, **114**, 598-604.
22. I. Shypunov, N. Kongi, J. Kozlova, L. Matisen, P. Ritslaid, V. Sammelselg and K. Tammeveski, *Electrocatalysis*, 2015, **6**, 465-471.
23. M. A. Kostowskyj, D. W. Kirk and S. J. Thorpe, *Int. J. Hydrog. Energy*, 2010, **35**, 5666-5672.
24. J. Liu, J. Liu, W. Song, F. Wang and Y. Song, *J. Mater. Chem. A*, 2014, **2**, 17477-17488.
25. H. Huang, Y. Meng, A. Labonte, A. Dobley and S. L. Suib, *J. Phys. Chem. C*, 2013, **117**, 25352-25359.
26. H. Erikson, A. Sarapuu and K. Tammeveski, *ChemElectroChem*, 2019, **6**, 73-86.
27. B. B. Blizanac, P. N. Ross and N. M. Marković, *J. Phys. Chem. B*, 2006, **110**, 4735-4741.
28. M. Luo, Z. Zhao, Y. Zhang, Y. Sun, Y. Xing, F. Lv, Y. Yang, X. Zhang, S. Hwang, Y. Qin, J. Y. Ma, F. Lin, D. Su, G. Lu and S. Guo, *Nature*, 2019, **574**, 81-85.
29. N. M. Marković, T. J. Schmidt, V. Stamenković and P. N. Ross, *Fuel Cells*, 2001, **1**, 105-116.
30. K. L. Pickrahn, S. W. Park, Y. Gorlin, H.-B.-R. Lee, T. F. Jaramillo and S. F. Bent, *Adv. Energy Mater.*, 2012, **2**, 1269-1277.
31. Y. Gorlin and T. F. Jaramillo, *J. Am. Chem. Soc.*, 2010, **132**, 13612-13614.
32. Y. Gorlin, C.-J. Chung, D. Nordlund, B. M. Clemens and T. F. Jaramillo, *ACS Catal.*, 2012, **2**, 2687-2694.

33. J. W. D. Ng, Y. Gorlin, D. Nordlund and T. F. Jaramillo, *J. Electrochem. Soc.*, 2014, **161**, D3105-D3112.
34. K. A. Stoerzinger, M. Risch, B. Han and Y. Shao-Horn, *ACS Catal.*, 2015, **5**, 6021-6031.
35. Y. Dessie, S. Tadesse, R. Eswaramoorthy and B. Abebe, *Journal of Science: Advanced Materials and Devices*, 2019, **4**, 353-369.
36. M. Rabe, C. Toparli, Y.-H. Chen, O. Kasian, K. J. J. Mayrhofer and A. Erbe, *Phys. Chem. Chem. Phys.*, 2019, **21**, 10457-10469.
37. Y. Gorlin, C. J. Chung, J. D. Benck, D. Nordlund, L. Seitz, T. C. Weng, D. Sokaras, B. M. Clemens and T. F. Jaramillo, *J. Am. Chem. Soc.*, 2014, **136**, 4920-4926.
38. Q.-m. Wu, J.-m. Ruan, Z.-c. Zhou and S.-b. Sang, *Trans. Nonferrous Met. Soc. China*, 2015, **25**, 510-519.
39. N. Fairley, V. Fernandez, M. Richard-Plouet, C. Guillot-Deudon, J. Walton, E. Smith, D. Flahaut, M. Greiner, M. Biesinger, S. Tougaard, D. Morgan and J. Baltrusaitis, *Appl.Surf. Sci.Adv.*, 2021, **5**, 100112.
40. M. C. Biesinger, B. P. Payne, A. P. Grosvenor, L. W. M. Lau, A. R. Gerson and R. S. C. Smart, *Appl. Surf. Sci.*, 2011, **257**, 2717-2730.
41. M. H. Engelhard, D. R. Baer, A. Herrera-Gomez and P. M. A. Sherwood, *J. Vac. Sci. Technol., A*, 2020, **38**, 063203.
42. A. Herrera-Gomez, M. Bravo-Sanchez, O. Ceballos-Sanchez and M. O. Vazquez-Lepe, *Surf. Interface Anal.*, 2014, **46**, 897-905.
43. A. A. Audi and P. M. A. Sherwood, *Surf. Interface Anal.*, 2002, **33**, 274-282.
44. T. Hofmann, T. H. Yu, M. Folse, L. Weinhardt, M. Bär, Y. Zhang, B. V. Merinov, D. J. Myers, W. A. Goddard and C. Heske, *J. Phys. Chem. C*, 2012, **116**, 24016-24026.
45. M. Newville, *J. Phys.: Conf. Ser.*, 2013, **430**, 1-7.
46. D. Nečas and P. Klapetek, *Open Phys.*, 2012, **10**, 181-188.
47. R. Zhou, Y. Zheng, M. Jaroniec and S. Z. Qiao, *ACS Catal.*, 2016, **6**, 4720-4728.
48. B. Hammer, L. B. Hansen and J. K. Nørskov, *Phys. Rev. B Condens. Matter Mater. Phys.*, 1999, **59**, 7413-7421.
49. G. Kresse and D. Joubert, *Phys. Rev. B*, 1999, **59**, 1758-1775.
50. G. Kresse and J. Furthmüller, *Phys. Rev. B*, 1996, **54**, 11169-11186.
51. H. J. Monkhorst and J. D. Pack, *Phys. Rev. B*, 1976, **13**, 5188-5192.

52. L. Wang, T. Maxisch and G. Ceder, *Phys. Rev. B*, 2006, **73**.
53. J. K. Nørskov, J. Rossmeisl, A. Logadottir, L. Lindqvist, J. R. Kitchin, T. Bligaard and H. Jónsson, *J. Phys. Chem. B*, 2004, **108**, 17886-17892.
54. G. T. K. K. Gunasooriya and J. K. Nørskov, *ACS Energy Lett.*, 2020, **5**, 3778-3787.
55. H. Li, S. Kelly, D. Guevarra, Z. Wang, Y. Wang, J. A. Haber, M. Anand, G. T. K. K. Gunasooriya, C. S. Abraham, S. Vijay, J. M. Gregoire and J. K. Nørskov, *Nat. Catal.*, 2021, **4**, 463-468.
56. I. Karakaya and W. T. Thompson, *J. Phase Equilib.*, 1990, **11**, 480-486.
57. M. H. Tang, C. Hahn, A. J. Klobuchar, J. W. D. Ng, J. Wellendorff, T. Bligaard and T. F. Jaramillo, *Phys. Chem. Chem. Phys.*, 2014, **16**, 19250.
58. L. Mao, D. Zhang, T. Sotomura, K. Nakatsu, N. Koshiba and T. Ohsaka, *Electrochim. Acta*, 2003, **48**, 1015-1021.
59. H.-Y. Su, Y. Gorlin, I. C. Man, F. Calle-Vallejo, J. K. Nørskov, T. F. Jaramillo and J. Rossmeisl, *Phys. Chem. Chem. Phys.*, 2012, **14**, 14010.
60. Y. Gorlin, B. Lassalle-Kaiser, J. D. Benck, S. Gul, S. M. Webb, V. K. Yachandra, J. Yano and T. F. Jaramillo, *J. Am. Chem. Soc.*, 2013, **135**, 8525-8534.
61. V. I. Birss, A. Damjanovic and P. G. Hudson, *J. Electrochem. Soc.*, 1986, **133**, 1621-1625.
62. W. Chen, Q. Xiang, T. Peng, C. Song, W. Shang, T. Deng and J. Wu, *iScience*, 2020, **23**, 101532.
63. Y. Yang, G. Chen, R. Zeng, A. M. Villarino, F. J. DiSalvo, R. B. van Dover and H. D. Abruña, *J. Am. Chem. Soc.*, 2020, **142**, 3980-3988.
64. Y. Yoon, B. Yan and Y. Surendranath, *J. Am. Chem. Soc.*, 2018, **140**, 2397-2400.
65. C. V. Cushman, P. Brüner, J. Zakel, G. H. Major, B. M. Lunt, N. J. Smith, T. Grehl and M. R. Linford, *Analytical Methods*, 2016, **8**, 3419-3439.
66. H. Li, K. Shin and G. Henkelman, *J. Chem. Phys.*, 2018, **149**, 174705.
67. P. Liu and J. K. Nørskov, *Phys. Chem. Chem. Phys.*, 2001, **3**, 3814-3818.
68. B. S. Yeo and A. T. Bell, *J. Am. Chem. Soc.*, 2011, **133**, 5587-5593.
69. R. Frydendal, M. Busch, N. B. Halck, E. A. Paoli, P. Krtil, I. Chorkendorff and J. Rossmeisl, *ChemCatChem*, 2015, **7**, 149-154.
70. Z. W. Seh, J. Kibsgaard, C. F. Dickens, I. Chorkendorff, J. K. Nørskov and T. F. Jaramillo, *Science*, 2017, **355**, 1-12.

71. G. T. K. K. Gunasooriya, M. E. Kreider, Y. Liu, J. A. Zamora Zeledón, Z. Wang, E. Valle, A.-C. Yang, A. Gallo, R. Sinclair, M. Burke Stevens, T. F. Jaramillo and J. K. Nørskov, unpublished work.
72. S. Back, M. H. Hansen, J. A. Garrido Torres, Z. Zhao, J. K. Nørskov, S. Siahrostami and M. Bajdich, *ACS Appl. Mater. Interfaces*, 2019, **11**, 2006-2013.
73. G. K. Wertheim, S. B. Dicenzo and D. N. E. Buchanan, *Phys. Rev. B*, 1986, **33**, 5384-5390.
74. S. Hüfner, G. K. Wertheim, N. V. Smith and M. M. Traum, *Solid State Commun.*, 1972, **11**, 323-326.
75. V. V. Nemoshkalenko, V. G. Aleshin, Y. N. Kucherenko and L. M. Sheludchenko, *J. Electron. Spectrosc. Relat. Phenom.*, 1975, **6**, 145-150.
76. B. Hammer and J. K. Nørskov, *Surf. Sci.*, 1995, **343**, 211-220.
77. J. K. N. Nørskov, F. Studt, F. Abild-Pedersen and T. Bligaard, *Fundamental Concepts in Heterogeneous Catalysis*, Wiley, Hoboken, New Jersey, 2014.
78. J. K. Nørskov, F. Abild-Pedersen, F. Studt and T. Bligaard, *Proc. Natl. Acad. Sci. U.S.A.*, 2011, **108**, 937-943.